This is the peer-reviewed, final accepted version for American Mineralogist, published by the Mineralogical Society of America.
The published version is subject to change. Cite as Authors (Year) Title. American Mineralogist, in press.
DOI: https://doi.org/10.2138/am-2022-8045. http://www.minsocam.org/

REVISION 1

Word Count: 9014

Hydrothermal mineralization of celadonite: hybridized fluid–basalt interaction in Janggi, Korea

Jongkyu Park[1,2], Hoseong Lim[3], Bora Myeong[4], Yun-Deuk Jang[1,2,*]

[1]Department of Geology, Kyungpook National University, Daegu 41566, Republic of Korea

[2]Research Institute for Dok-do and Ulleung-do Island, Daegu 41566, Republic of Korea

[3]School of Earth, Atmosphere and Environment, Monash University, 3800 Clayton, VIC, Australia

[4]GeoZentrum Nordbayern, Universität Erlangen-Nürnberg, Schloßgarten 5, 91054 Erlangen, Germany

*Corresponding author. Telephone: +82-53-950-5354. E-mail: jangyd@knu.ac.kr

ABSTRACT

The origin of celadonite still remains enigmatic and fragmentary. Exceptional celadonite mineralization was discovered in the Miocene lacustrine Janggi Basin in the southeastern Korean Peninsula. This Janggi celadonite is a greenish earthy/vitreous material filling the E–W trending fault zones in basaltic flows. The scale of the celadonite body is up to a meter thick and laterally extends approximately 10 m. These occurrences are markedly in contrast with celadonite as

vesicle-filling or mineral-replacing types in the literature. The Janggi celadonite allows exploring the puzzling genesis of celadonite and comparing its characteristics with global cases for a better understanding of celadonite formation.

X-ray diffraction and micro-probe analyses demonstrate that the Janggi celadonite ranges from ferroceladonite–celadonite–ferroaluminoceladonite and is mixed with opal at a ratio of up to ~3:7. Detailed field work and whole-rock major, trace, and oxygen isotope analyses indicate that celadonite is formed in an open system of ~120°C by the interaction of hybridized fluid (a mixture of <55% magmatic and >45% other origins) and basalts during the physicochemical fault brecciation of the host rock. The cations needed for celadonite formation were supplied from the smectitization/zeolitization of rhyolitic mesostasis (for Al and part of K) and pyroxene microlites (for Fe and Mg) in the basaltic breccias during the associated oxidation of micro–nanoparticles by circulating fluids (for most of K).

A comparison of the Janggi celadonite with global cases highlights that celadonite genesis is neither limited to the seawater alteration of basalt nor do hosts and reactive fluids control celadonite compositions. A contextualized perspective on celadonite genesis alludes that a potassic alteration of rock that is rich in ferromagnesian components in a shallow crustal environment (<~200 MPa at <~450°C) produces celadonite. Because of the relative availability of the necessary components for celadonite precipitation, our model expects celadonite mineralization in many volcanic environments, where magmatic fluid and particle size reduction could contribute. These insights emphasize celadonite's potential applications for tracing geothermal history.

Keywords: Celadonites; Hydrothermal mineralization; Fault brecciation; Fluid–rock interaction;

Oxygen isotope

INTRODUCTION

Celadonite is a 2:1 dioctahedral true mica with a general formula of $KR^{3+}R^{2+}Si_4O_{10}(OH)_2$ (Rieder et al. 1998). Because of the complex homo- or heterovalent cation substitution in octahedral sites, its compositional variety has been reported to be ferroceladonite–ferroaluminoceladonite (Li et al. 1997), aluminoceladonite (Drits et al. 2010), and magnaniceladonite (Lepore et al. 2017) endmembers.

Celadonite commonly occurs as greenish vesicle-lining or vesicle-filling materials in highly porous basalts (e.g., Baker et al. 2012) and occasionally as replacement phases for various ferromagnesian minerals, such as olivine (Laverne et al. 2006), pyroxene (Alt et al. 2010), amphibole (Barzoi and Seclaman 2010), biotite (Keeling et al. 2018), and Fe-$(OH)_x$ (Schramm et al. 2005). Celadonite has long been regarded as a product of the *seawater alteration of basalt* in marine environments (e.g., Alt et al. 2010; Andrews 1980; Böhlke et al. 1984; Marescotti et al. 2000; Odin et al. 1988; Talbi and Honnorez 2003; Teagle et al. 1996) (Table 1). However, this genetic consensus has been challenged by recent works. For example, celadonite is observed as a product of groundwater alteration (Baker et al. 2012; Innocent et al. 1997; Renac et al. 2010), deuteric alteration of basalt (Schenato et al. 2003), and microbial activity within basalt (Reolid and Abad 2014) (Table 1). Furthermore, the host rock spectrum of celadonite is significantly broad, ranging from basaltic (Baker et al. 2012), andesitic (Cathelineau and Izquierdo, 1988), and rhyolitic volcanic rocks (Li et al. 1997) to sedimentary (Tóth et al. 2010) and metamorphic rocks (Keeling et al. 2018) (Table 1).

Tracking the source of cations and fluids needed for celadonite precipitation would provide a plausible forming mechanism because celadonite genesis has many possible routes (not limited to one of those above) that must be carefully constrained to extract geological implications. Therefore, various aspects of approaches on celadonite and its hosts should be integrated to obtain their mineral, whole-rock, and isotopic characteristics. However, in many cases, at least one of the essential aspects is missing.

Exceptional celadonite mineralization was discovered in the Miocene lacustrine Janggi Basin in the southeastern Korean Peninsula. The Janggi celadonite is deposited as a fault-filling greenish earthy/vitreous material of up to a meter thick and ~10 meters lateral continuity along the fault zones developed in their basaltic host. Mega-scale celadonite mineralization and its lacustrine forming environment are in contrast with general cases in the literatures (i.e., vesicle-filling/mineral replacement in a marine environment) (Table 1). A unique forming mechanism regarding the volume of celadonite mineralization in the study area is expected, which would provide insight into the celadonite genesis in other geological settings.

We report a detailed description of the Janggi celadonite in order to delineate the celadonite mineralization mechanism. The mineral, whole-rock, and oxygen isotopic characteristics are comprehensively combined to trace the sources of cations and, especially, fluids. In addition, these characteristics are compared with global cases to better understand how and under what conditions celadonite forms.

GEOLOGICAL OUTLINE

Several Miocene pyroclastic–sedimentary basins, such as the Early Miocene lacustrine Janggi,

Waeup, Eoil, Haseo, Jeongja, Ulsan, and Middle Miocene marine Pohang Basins, are distributed in the southeastern Korean Peninsula (Fig. 1a; Sohn et al. 2013; Son et al. 2015). These basins are constrained by NNE-trending normal and NNW-trending dextral strike-slip faults along their western boundaries, which are interpreted to be the result of the pull-apart extension related to the opening of the East Sea (Son et al. 2015; Fig. 1a).

The study area is the central part of the Early Miocene lacustrine Janggi Basin (Fig. 1b), which has a lithostratigraphy consisting of lower dacitic–rhyolitic (22.7–19.8 Ma) and upper basaltic (22.1–18.0 Ma) volcanics underlain by the Cretaceous–Eocene basement (Kim et al. 2011; Shin 2013). The Miocene dacitic–basaltic rocks with a calc-alkaline magma evolutionary trend extruded over a volcanic-arc setting (Choi et al. 2013; Kim et al. 2011; Park et al. 1999; Shim et al. 2011).

METHODS

Field works and petrography

A 1:5,000 geological map was made during detailed field work, on which the orientations of celadonite deposits were measured. In total, 125 samples were obtained, among which 43 representative samples were prepared as traditional polished thin sections. The mineral abbreviations in the figures follow those from Whitney and Evans (2010).

X-ray diffraction (XRD)

Fault-filling bulk celadonite samples were selected. A tungsten carbide ball mill was used to crush the samples into pieces with smaller than 1 mm size in diameter for 30 s. After then, the samples were powdered using an agate mortar and pestle for ~2 min. To concentrate the clay fraction, the

powdered samples were suspended in individual deionized water columns and separated by gravity settling for 3 h (Li et al. 1997). After the concentration, air-dried random powder samples were made through the back-loaded method (Moore and Raynolds 1989). These samples were analyzed using an X'pert Pro-MPD diffractometer at the Daegu Center of the Korea Basic Science Institute. The analytical conditions were as follows: CuK_a radiation at 40 kV, 30 mA, 5–70 2θ°, 0.02°/s. The cell parameters were calculated using the UnitCell software devised by Holland and Redfern (1997) and summarized in Table 2. Semi-quantification of scans was conducted using SIROQUANT v.3.0 software. For the CELA-1 sample, an additional oriented sample was prepared through the glass slide method (Moore and Raynolds 1989). This sample was air-dried at room temperature and treated as ethylene glycol vapor in a 65°C oven for 24 h to check smectite (Mosser-Ruck et al. 2005). The sample at each step (air-dried and ethylene glycol treatment) was analyzed at the same institute. The analytical conditions were as follows: CuK_a radiation at 40 kV, 30 mA, 2–40 2θ°, 0.02°/3s.

Whole-rock major, trace elements, and oxygen isotope analysis

The representative fresh basaltic rocks and celadonites were crushed and powdered. Whole-rock analyses were conducted at Activation Laboratories (Ontario, Canada) using fusion-inductively coupled plasma (FUS-ICP; Thermo Jarrel-Ash ENVIRO II) for major elements and ICP mass spectrometry (ICP-MS; Perkins Elmer Sciex ELAN 6000) for trace elements. The analytical error ranges for the major (>1 wt%) and trace elements were <~2% and <10%, respectively (Electronic Supplementary Material (ESM) 1). Oxygen isotope compositions were obtained from fresh and altered basaltic rocks and celadonites at the same laboratory using an isotope ratio mass

spectrometer (Finnigan MAT Delta). The data are reported as the δ notation relative to the Vienna Standard Mean Ocean Water (V-SMOW), which had an analytical error range of <3% (ESM 1).

Electron micro-probe (EMP) analysis

Mineral chemistry (ESM 2) was acquired using a JEOL JXA-8530F EMP with wavelength-dispersive spectrometers at the Kyungpook National University Scientific Instruments Center. EMPA was conducted using an accelerating voltage of 15 kV, a beam current of 20 nA, beam size of 3–5 μm, and durations of 20 s and 10 s for peak and background positions, respectively. The standard materials used for the analysis were albite (Na), almandine (Fe), apatite (P), diopside (Ca), periclase (Mg), pyrope (Al), quartz (Si), rhodonite (Mn), rutile (Ti), and sanidine (K). During the analysis, the standard and additional international and in-house minerals were duplicated as unknown sample sets to assess the data quality. Furthermore, the analytical error ranges of each element converged within ~2% for elements with an abundance of >1 wt% (ESM 2).

Structural formula calculation and data compilation for celadonite

Structural formulas for celadonite compositions obtained during this study were normalized to a 22+ charge after conversion of the total iron content to ferric iron; celadonite is Fe^{3+}-rich dioctahedral mica (Li et al. 1997). After normalization, all Si cations were assigned to tetrahedral sites, and the remaining sites were filled with Al up to $\sum^{IV}R = 4$. Fe, Mg, Ti, Mn, and the residual Al cations were allocated into octahedral sites, and K, Na, Ca, and P into interlayer sites. After the cation allocation, the tetrahedral, octahedral, and interlayer cations were re-normalized to 4, 2, and 1, respectively (Li et al. 1997; Wise and Eugster 1964). The ferric-ferrous ratios in the octahedral

sites were estimated to achieve stoichiometry (Baker et al. 2012; Li et al. 1997). ESM 3 also compiles the published celadonite whole-rock and mineral compositions. The structural formulas of the published celadonite mineral compositions were calculated following the same protocol for comparison.

RESULTS

Field geology and petrography

Volcanics. The lower stratigraphic level of the study area consists of dacitic–rhyolitic lapilli tuff (Fig. 1b), which is a bright gray to yellowish brown massive to stratified unit interlayered with lacustrine tuffaceous sediments (Fig. 2a). This unit has angular quartz, plagioclase, biotite, and pumice (Fig. 2b) and locally contains accidental lithic fragments ranging from andesite to rhyolite (Kim et al. 2011).

Basaltic volcanics cover the dacitic–rhyolitic lapilli tuff over a discordant boundary. These rocks can be divided into four sub-units (Fig. 1b) based on their field relationships and petrographic characteristics. In ascending order from the lower to the upper level, these sub-units are basaltic tuff breccia (Fig. 2c), trachytic (in a descriptive and textural sense) basalt (Figs. 2d and e), porphyritic basalt (Figs. 2f and g), and intrusive microcrystalline basalt (Figs. 2h and i). These basaltic rocks are dark to light gray and contain euhedral–subhedral plagioclase, clinopyroxene phenocrysts (>0.5 mm), and microlites (<0.5 mm) as major phases, with occasional olivine microlites (Figs. 2e and g).

The basaltic tuff breccia exposed in the center of the study area (Fig. 1b) is a locally grain- or matrix-supported unit with irregular lateral and vertical variations (Kim et al. 2011). The main

body of trachytic basalt is in the northwestern part of the study area (Fig. 1b) with flow joints that gently dip south to southwest (Fig. 2d), which is a key feature in distinguishing trachytic and porphyritic basalts. The porphyritic basalt covers the lower units with irregular boundaries in the northern area (Fig. 1b) and is characterized by phenocrysts ranging from 1.0 to 7.0 mm (Fig. 2g). The microcrystalline basalt intrudes the trachytic and porphyritic basalt flows in the southwestern part of the study area (Fig. 1b) and is characterized by irregular columnar joints and a paucity of phenocrysts (Figs. 2h and i).

Celadonite. Celadonite in the study area has a broad range of occurrences, including a vesicle-filling and fault/fracture-filling material with an earthy (Figs. 3a and b) or vitreous luster (Figs. 3c–e) in trachytic basalt. Vesicle-filling celadonite is rarely observed because of the paucity of vesicles in basaltic hosts. Fault-filling earthy celadonite with an E-W orientation is the most common type and contains reddish altered trachytic basalt fragments with mosaic fabric (Figs. 3a and b).

Other minor fault/fracture-filling materials such as carbonates (mainly calcite) and quartz (mainly opal) are also present. Carbonates have sharp boundaries with the celadonite rather than occurring as a mixture with celadonite (Fig. 3d). The quartz veins grade into the vitreous celadonite (Fig. 3e), and occur as a mixture with celadonite like the green opal of Bustillo and Martinez-Frias (2003) in Tenerife, Canary Islands.

To identify mineralogical characteristics, XRD analysis for the earthy (CELA-1) and vitreous (CELA-2 and CELA-3) samples was conducted (Fig. 4). The XRD results, especially those derived from CELA-1 (Fig. 4), are consistent with the published celadonite peaks (Table 2; Baker et al. 2012; Buckley et al. 1978; Li et al. 1997; Odin et al. 1988). The XRD pattern of celadonite is

similar to that of glauconite because of crystallographic similarity (See also ESM 4). However, the samples have a $d_{(060)}$ peak of <1.510 Å (Fig. 4), which confirms celadonite (cf. $d_{(060)}$ of glauconite >1.510 Å; Buckely et al. 1978). Meanwhile, the CELA-2 and CELA-3 samples are mixed with opal to greater degrees compared to the CELA-1 sample (Fig. 4). This characteristic is represented by the peak band between 16 and 32 2θ° (e.g., Bustillo and Martinez-Frias 2003). According to Herdianita et al. (2000), the opaline material is subdivided into opal-A, opal -CT, and opal -C with distinct XRD peak characteristics. Considering the peak characteristics, the celadonite samples of this study contain celadonite, microcrystalline quartz, opal-CT (at ~20.64, 21.55, and 35.45 2θ°), opal-A (at 16–32 2θ°), and trace or absence of smectite (i.e., no shift of the $d_{(001)}$ peak of the ethylene glycol-treated CELA-1) in descending order of content (Fig. 4). Consequently, a higher opal content causes a more vitreous luster (Figs. 3 and 4).

Celadonites with varying opal content are yellowish-green to pale-green, and display weak pleochroism under PPL (Fig. 5a) and blue-greenish to dark-green interference colors under XPL (Fig. 5b). These results are consistent with the optical features of celadonite reported by Marescotti et al. (2000). The fragments of trachytic basalt and their rock-forming minerals are suspended in a celadonite matrix (Figs. 5a and b). The mesostasis of basaltic fragments is altered to a reddish color (Fig. 5a), corresponding to the brown alteration halo that Alt and Teagle (2003) observed at the ODP 801 site. Celadonite is injected into the cleavage/parting of clinopyroxene and the sieve structure of plagioclase phenocrysts (Figs. 5c and d), showing sharp boundary characteristics under BSE images. Although significant alteration halos surrounding the celadonite injection are not observed, a sub-microscale replacement can not be ruled out.

Whole-rock geochemistry

Major elements. The volcanics in the study area follow a sub-alkaline evolutionary path with bimodal populations in the total alkali versus silica (TAS) diagram (Fig. 6a). The dacitic–rhyolitic lapilli tuff is in the trachyte through dacite to rhyolite fields, whereas the basaltic volcanics are basalt to basaltic andesite (Fig. 6a). With an increased SiO_2 content, Al_2O_3, Fe_2O_{3t}, MgO, MnO, CaO, TiO_2, and P_2O_5 decrease, but K_2O increases (Figs. 6b–e).

The Janggi celadonite contain SiO_2 (64.94–75.39 wt%), Al_2O_3 (4.18–7.60 wt%), Fe_2O_{3t} (5.49–13.23 wt%), MgO (2.38–4.75 wt%), and K_2O (2.86–4.77 wt%) as major components (Figs. 6b–e). Other oxides such as TiO_2 (0.12–0.35 wt%), MnO (0.02–0.04 wt%), CaO (0.29–0.76 wt%), Na_2O (0.12–0.45 wt%), and P_2O_5 (0–0.05 wt%), have abundances of <~1 wt%. The high SiO_2 abundances of celadonite reflect the admixture with opal, consistent with the XRD data (Fig. 4) and comparison to the relatively pure celadonite of Odin et al (1988) and the celadonite-opal mixture of Bustillo and Martinez-Frias (2003) (Figs. 6b–e).

Trace elements. Figure 7a shows the chondrite-normalized trace element patterns for the volcanics in the study area. The basaltic volcanics are enriched with large ion lithophile elements (Rb, Ba, and Th) and light rare earth elements (La, Ce, Pr, and Nd) relative to mid-ocean ridge basalt (MORB) (Fig. 7a). This has been explained by their subduction-related genesis (e.g., Choi et al. 2013). The dacitic–rhyolitic volcanics have similar trace element patterns but are more enriched than the basaltic volcanics (Fig. 7a). The major and trace element characteristics in this study (Figs. 6 and 7a) indicate that these rocks share a common volcanic lineage.

The trace element patterns for the Janggi celadonite are considerably similar to those of the basaltic volcanics (Fig. 7b). For example, the three-fold values of the mean of CELA-1 and CELA-2 are

in the basaltic volcanic field (i.e., the modeled celadonite in Fig. 7b). Except for Rb, the trace elements are relatively depleted compared to the basaltic volcanics (Fig. 7b), and the degree of depletion seems to be controlled by the quartz/opal content (cf. Tóth et al. 2010). In addition, the extremely high Rb content of the celadonite samples (Fig. 7b) is attributed to the substitution of Rb for K in the celadonite interlayer sites (e.g., Booij et al. 1995; Innocent et al. 1997).

Oxygen isotope. Figure 8 shows the Oxygen isotope compositions. The $\delta^{18}O_{V\text{-}SMOW}$ values from the fresh basaltic volcanics are 5.74–7.08‰ (Fig. 8), which are slightly higher than those of typical MORB (5.37–5.81‰; Eiler et al. 2000). The reddish altered basaltic fragments within celadonite veins have the broadest $\delta^{18}O_{V\text{-}SMOW}$ range at 9.77–16.16‰ (Fig. 8). The celadonite is between fresh and altered basalts, ranging from 9.40 to 12.41‰. The $\delta^{18}O_{V\text{-}SMOW}$ values of the Janggi celadonite are comparable to those from the Kerguelen Archipelago (Renac et al. 2010) and DSDP Leg 81 (Odin et al. 1988) (Fig. 8).

Mineral chemistry

Pyroxenes. Pyroxene phenocrysts from the fresh basaltic volcanics (Fig. 9a) and reddish altered basalt fragments (Fig. 9b) are augite with an almost identical composition, having Mg# (Mg / (Mg + Fe^{2+} + Fe^{3+})*100) of 76.73–64.65 and 70.51–64.34, respectively. The pyroxene microlites of the basaltic volcanics have augitic to enstatitic compositions with a broad Mg# of 73.48–46.76 (Fig. 9c). However, pyroxene microlites were not observed in the altered basaltic fragments.

Mesostasis. Fresh mesostasis from the basaltic volcanics (Fig. 9c) has a rhyolitic composition (Fig. 6a), of which the main components are SiO_2 (78.05–81.11 wt%), Al_2O_3 (11.08–13.26 wt%), K_2O (2.62–4.13 wt%), and FeO (0.86–2.98 wt%), with other elements in abundances of <2 wt%.

On the other hand, mesostasis from the reddish altered basaltic fragments (hereafter, altered mesostasis; Fig. 9b) has a significantly broader compositional range of SiO_2 (43.54–83.85 wt%), Al_2O_3 (0.09–5.33 wt%), K_2O (0.13–4.78 wt%), FeO (2.92–16.21 wt%), and MgO (0.01–19.46 wt%) (ESM 2).

Celadonite. The Janggi celadonite is classified as ferroceladonite–celadonite–ferroaluminoceladonite regardless of their luster (Fig. 10a). The mixing characteristics of celadonite and opal (Fig. 9d) up to ~3:7 negligibly affect the classification (Fig. 10b; ESM 4). Celadonite compositions with <60 wt% SiO_2 and >8.5 wt% K_2O (i.e., being considered as relatively pure celadonite, Fig. 10b) show low ^{IV}Al abundances of 0.06–0.18 atoms per formula unit (apfu) (ESM 2), which is consistent with the general interpretation that celadonite has ^{IV}Al less than 0.2 apfu (Baker et al. 2012; Velde 1972; Wise and Eugster 1964). For opal-rich celadonite (with >60 wt% SiO_2 and <8.5 wt% K_2O), the cation allocation and re-normalization procedure slightly overestimate the octahedral Al abundances up to ~0.2 apfu (ESM 4) because the tetrahedral sites are completely filled with Si (thus, all Al cations are allocated to the octahedral sites). However, this approximation does not change our celadonite classification result (Fig. 10a; ESM 4).

DISCUSSION

Comparison to global celadonite occurrences

Lithological perspective. The diverse host lithology, especially rhyolitic tuff (Table 1), allowed us to question why no celadonite exists in the dacitic–rhyolitic lapilli tuff in the study area (Fig. 2a), as celadonites in andesitic–rhyolitic tuff of the Hokonui Hills in New Zealand (Li et al. 1997)

have been reported. Furthermore, the dacitic–rhyolitic lapilli tuff in the Janggi area (Fig. 2a) underwent significant zeolitization during diagenesis within a lacustrine environment (Noh and Boles 1989), liberating various cations into solution. Therefore, the inference that dacitic–rhyolitic lapilli tuff in the Janggi area might bear celadonite must be discussed.

Plagioclase, biotite, and Fe–Ti-oxide phenocrysts in the dacitic–rhyolitic lapilli tuff were not affected by zeolitization (Fig. 2b), however, its dacitic glass shards were hydrated and dissolved to precipitate authigenic K-feldspar (Noh and Boles 1989). This paragenesis indicates the two critical constraints: (1) Zeolitization within dacitic–rhyolitic lapilli tuff in the study area could not supply enough ferromagnesian and alumino components to form celadonite due to the intactness of the phenocrysts, and (2) K from the dacitic glass shards was exhausted to precipitate authigenic K-feldspar rather than celadonite (Laureijs et al. 2021). These nutrient deficiencies explain the absence of celadonite in the dacitic–rhyolitic lapilli tuff and, perhaps, the poor occurrence of several micrometer-scaled celadonite of Li et al. (1997) within tuffs with compositions similar to those in this study.

Faulting perspective. The Janggi celadonite contains numerous trachytic basalt fragments with mosaic fabric and has systematic E-W orientations (Fig. 3). There are no significant alteration halos around celadonite veins toward the adjacent trachytic basalt host, however, the basaltic fragments within the veins have varying degrees of alteration characteristics (Fig. 3b). These observations suggest that the celadonite-forming process in this study is deeply associated with physicochemical fault-related brecciation and accompanying hydrothermal mineralization (e.g., Jébrak 1997) at various depths.

Despite extensive celadonite deposits in the Troodos in Cyprus (e.g., Booij et al. 1995; Gallahan

and Duncan 1994), a mechanical celadonite-forming model for that area has not yet been reported. However, the occurrence of Janggi celadonite would be a critical analogue for conceiving the genesis of Troodos celadonite because an intensive fault zone development that occurred during the uplift of Troodos ophiolite (e.g., Ring and Pantazides 2019) is suspected to have induced a similar fault-related brecciation to that noted in this study.

Whole-rock geochemical perspective. The fault brecciation of the host (Fig. 3a) indicates that the source materials of the Janggi celadonite would mainly be derived from basaltic rocks. This inference is supported by the trace element patterns of celadonite being remarkably similar to those of basaltic rocks (Fig. 7b). However, the celadonite shows a more significant negative Eu anomaly (i.e., $(Eu / ((Sm + Gd) / 2)_{CN}$; 0.55–0.86) than the basaltic rocks (0.78–1.03), indicating that plagioclase has a limited role in the celadonite-forming process (Cummings et al. 1989). For comparison, Tóth et al. (2010) analyzed the REEs of celadonite from manganese black shale in Hungary, and those patterns are similar to that of Post-Archean Australian average Sedimentary rock (PAAS; Fig. 7b). These examples imply that the REEs of celadonites are inherited from the host rocks (i.e., the origin of the source material) because the REEs have similar charges and ionic radii, which leads to coherent geochemical behavior during the alteration process (e.g., Bau 1996; Hajash 1984; Wood et al. 1976).

Mineralogical perspective. The octahedral sites of the celadonite lattice are filled with di- and trivalent cations through homo- and/or heterovalent cation substitution (e.g., Wise and Eugster 1964; Li et al. 1997). These cation variations (e.g., Laverne et al. 2006; Marescotti et al. 2000; Talbi and Honnorez 2003) hinder determining whether their compositional variety resulted from cation substitution or phase mixing/interlamination. In this context, K_2O content representing the

interlayer sites can be used to confirm the mixing relationship of celadonite with other phases (Fig. 10b) because the interlayer sites are relatively less affected by complex substitution than octahedral sites.

The Janggi celadonite has a broad compositional range that is disseminated around the center of the classification diagram (Fig. 10a), indicating that the components needed to precipitate celadonite were easily and congruently supplied. In addition, as expected from the XRD and whole-rock geochemical results (Figs. 4 and 6), there is a conspicuous mixing trend of celadonite and opal without a significant smectite involvement (Fig. 10b).

The celadonite resulting from seawater alteration of basalts is classified as ferroceladonite–celadonite and concentrated along the upper boundary of the diagram (Fig. 10a). This distribution is considered to be a substantial interlamination of K-poor smectites, such as saponite (Talbi and Honnorez 2003) and/or nontronite (Böhlke et al. 1984) within celadonite layers, which is supported by the well-defined Cel-Sm mixing trend (Fig. 10b).

The celadonite related to groundwater alteration of basalts is mainly classified as celadonite–ferroaluminoceladonite (Fig. 10a). These celadonites show an intermediate trend between the Cel-Sm and Cel-Opl mixing lines (Fig. 10b), which is consistent with the celadonite-opal-smectite-zeolite assemblage noted by Baker et al. (2012). Although Innocent et al. (1997) and Schenato et al. (2003) have interpreted the celadonite of the Parana Basin in Brazil as resulting from groundwater and deuteric alteration, respectively, celadonites in those areas could have originated from independent forming environments/conditions, as their study areas were far apart.

Celadonite associated with microbial activity (Reolid and Abad 2014) has relatively higher Mg and Al contents than others (Fig. 10a), which is probably due to an interlamination of glauconite

(i.e., Mg-rich than celadonite) within their samples. Reolid and Abad (2014) reported a textural transition from glauconite to celadonite within a ~20 μm scale and explained celadonite as the most evolved stage of glauconitization. Furthermore, their XRD results show celadonite and glauconite peaks together in a sample.

Constraining celadonite-forming conditions

By comparing global celadonite occurrences (Table 1), we stress that the celadonite manifestation is not confined to basaltic rocks and the associated seawater alteration, and that their mineralogical compositions are not controlled by host rocks and reactive fluids (Fig. 10). This perspective is in contrast with the prevailing interpretation that celadonite is formed by the seawater alteration of basaltic rocks. Therefore, the celadonite-forming conditions should be examined more carefully.

Experimental and empirical constraints. A mineral's stability field is commonly constrained within an experimental P-T-t-X space. A few experimental studies have reported the following P-T conditions for the celadonite stability field, namely, <430°C at 100–200 MPa (Wise and Eugster 1964) and 300–400°C at 10–450 MPa (Velde 1972). They also pointed that the celadonite stability field is scarcely affected by pressure. Furthermore, Muller et al. (2000) performed dehydroxylation experiments on celadonite up to 650°C. These experiments indicate that the upper thermal stability field of celadonite might be extended to a late-magmatic hydrothermal temperature (~450°C at least). Booij et al. (1995) reported that the timing of the Troodos celadonite precipitation was almost identical to that of the eruption of their basaltic host rocks, indicating that celadonite can be precipitated within a very short geological time scale. These points imply that the thermal conditions and the sources of chemical components are far more critical for the celadonite genesis

than the pressure and timing conditions.

Thermal conditions. Celadonite precipitation temperature would be estimated using oxygen isotope thermometry (e.g., Alt et al. 2010; Alt and Teagle 2003; Böhlke et al. 1984; Renac et al. 2010). Applying oxygen isotope thermometry requires an equilibrium of coexisting phases and their isotopic compositions. Opal coexisting with celadonite (Fig. 9d) is comparable to the excess SiO_2 noted by Wise and Eugster (1964), which indicates the attainment of equilibrium of celadonite-opal-fluid at the time of precipitation (See also Laureijs et al. 2021). Because our celadonite is mixed with opal (Fig. 4), the $\delta^{18}O_{V\text{-}SMOW}$ values of *pure celadonite* and *pure opal* can be extrapolated through their relative abundances (Fig. 11). In Figure 10b, the SiO_2 and K_2O abundances were designated as proxies for opal and celadonite, respectively. Therefore, for example, $\delta^{18}O_{V\text{-}SMOW}$ vs. SiO_2 wt% represents a relationship between oxygen isotope and opal content (Fig. 11), through which the $\delta^{18}O_{V\text{-}SMOW}$ of pure celadonite (at 54.52 wt% SiO_2) and opal (at 90.00 wt% SiO_2) can be estimated. The celadonite and opal ratios, estimated from XRD results (Fig. 4), can be used similarly (Fig. 11). Consequently, we use the $\delta^{18}O_{V\text{-}SMOW}$ of 8.21‰ and 15.18‰ for representing celadonite and opal, respectively (Table 3).

Modifying the general equation of mineral-water oxygen isotope thermometry for temperature versus $\delta^{18}O_{V\text{-}SMOW}$ of fluid compositions (ESM 3), figure 12 shows celadonite-H_2O (Sheppard and Gilg 1996) and opal-H_2O (Clayton et al. 1972; Zhang et al. 1989) oxygen isotope fractionation curves. Given the attainment of celadonite-opal-fluid equilibrium, the crossing point of Cel-water and Opl-water curves represent the thermal condition (~120°C) and oxygen isotope composition of the fluid (~-3.6‰ $\delta^{18}O_{V\text{-}SMOW}$) at the time of celadonite and opal co-precipitation (Fig. 12). The

This is the peer-reviewed, final accepted version for American Mineralogist, published by the Mineralogical Society of America.
The published version is subject to change. Cite as Authors (Year) Title. American Mineralogist, in press.
DOI: https://doi.org/10.2138/am-2022-8045. http://www.minsocam.org/

thermal estimation of ~120°C is compatible with published works (i.e., ~15–200°C) using oxygen isotope thermometry (Table 1; Alt et al. 2010; Alt and Teagle 2003; Böhlke et al. 1984; Renac et al. 2010). The identity of the estimated fluid composition of ~-3.6‰ $\delta^{18}O_{V\text{-}SMOW}$ will be constrained in the following section.

Tracking sources. Figure 3a and 7b indicate that the main components of celadonite (Si, Fe, Al, Mg, and K) are derived from trachytic basalt (i.e., a closed system). The textural difference between fresh and reddish altered trachytic basalts is manifest in their matrix (Figs. 9a–c), suggesting that the essential components for celadonite formation originate from their rhyolitic mesostasis (for Si, Al, and K; Noh and Boles 1989) and pyroxene microlites (for Fe and Mg; Baker et al. 2012) rather than the phenocrysts. In particular, Fe^{3+} versus Fe^{2+} variations of celadonite and pyroxene microlites show that Fe^{2+} from the pyroxene microlites is oxidized to Fe^{3+}, providing the essential ferric component for celadonite (ESM 5).

Although a closed system (i.e., alteration of basalt itself) alone can not explain the extensive amounts of celadonite precipitation, it provides most of the ferromagnesian and *partial* K components. This is because the pyroxene microlites within the reddish altered basaltic fault breccia are completely dissolved (Fig. 9b), and the altered mesostasis trends toward smectite have a decreasing K_2O content relative to the fresh mesostasis (Fig. 10b) (e.g., Meunier et al. 2008; Porter et al. 2000). The fresh mesostasis (3.50 wt% K_2O in average; ESM 2) provides only ~1/3 of the K required for the pure celadonite (9.45 wt% K_2O in average; ESM 2) with <60 wt% SiO_2 (Fig. 10b). Thus, the celadonite-forming process in the study area requires a large and open system. In this context, a problem regarding fluid origin arises.

The fluid composition of ~-3.6‰ $\delta^{18}O_{V\text{-}SMOW}$ is crucial for tracking its source. Studies on

celadonite have reported the influence of several reactive fluids such as seawater (Alt et al. 2010; Dudoignon et al. 1989), groundwater (Renac et al. 2010), and deuteric water (Schenato et al. 2003). However, the potential fluid of ~-3.6‰ $\delta^{18}O_{V\text{-}SMOW}$ strongly indicates the essential involvement of the magmatic fluid (e.g., 55% magmatic fluid and 45% groundwater) because no other mixing combinations, except for the magmatic fluid, can produce a value of ~-3.6‰ $\delta^{18}O_{V\text{-}SMOW}$ (Fig. 12). Although a counter endmember to the magmatic fluid might have supplied some K, a late-magmatic hydrothermal fluid is more likely to have provided most K to precipitate celadonite. Furthermore, the observation that celadonite samples have high silica content (Figs. 4, 6, and 10) indicates that the fluid was rich enough in Si to deposit large amounts of opal. Thus, the fluid probably had a late-magmatic hydrothermal affinity rather than meteoric or seawater origins (Fig. 12).

Laureijs et al. (2021) recently reported that the increasing fluid Si content significantly extends the celadonite stability field based on Eh-pH phase equilibrium modeling. The Janggi celadonite would be a tangible evidence of the conceptual model because of the intensive celadonite mineralization (Fig. 3) and its co-precipitation with opal (Figs. 4, 10, and 12).

IMPLICATIONS

Figure 13 is a schematic illustration of a celadonite-forming model based on the previous discussions. Following basaltic volcanism (22.1–18.0 Ma) until ~15 Ma, the study area was in an NNW-SSE extensional setting (Kim et al. 2011; Son et al. 2015). Within this setting, the E-W-trending fault activities reduced the basaltic fault breccia grain size to micro–nanoparticles (e.g., Verberne et al. 2019; Fig. 13a). This process facilitated the open system reaction of the particles

with a fault-injected hydrothermal fluid toward the oxidation front at ~120°C (Fig. 13b). These physicochemical conditions can provide a suitable environment for promoting significant celadonite precipitation in the study area (Figs. 3 and 13).

The forming model proposed in this study implies that celadonite was formed by smectitization/zeolitization of rhyolitic mesostasis (Noh and Boles 1989) and pyroxene microlites (Baker et al. 2012) in basaltic rock along with the accompanying oxidization of the basalt-derived micro–nanoparticles by reactive hybrid fluids (<55% magmatic and >45% other origins) within the fault zone (Fig. 13). This model suggests that any crustal rocks (i.e., not restricted to basalts) rich in ferromagnesian components could produce celadonite through hydrothermal potassic alteration.

The model proposed in this study predicts that there might be a celadonite with much dominant and clear magmatic signatures than our case. If any, celadonite with magmatic signatures can be precipitated from a fluid of higher temperature than our case, because celadonite is stable up to at least ~450°C (Muller et al. 2000; Velde 1972; Wise and Eugster 1964). This celadonite-forming mechanism is plausible, where both the magmatic fluid influx and particle size reduction could be involved like the fault-related milling in this study. A hydrothermal fluid-induced explosive eruption (e.g., Montanaro et al. 2020) or a peperite-related fragmentation (e.g., Skilling et al. 2002) would be that case. For example, the explosive volcanic succession of the Lake Okaro (New Zealand) contains greenish altered clasts (Montanaro et al. 2020). Celadonite has indeed been observed along the contacting peperites between lava and wet sediments in the northern Parana Basin (Brazil) (Moraes and Seer 2018). In addition, Pałgan et al. (2016) reported that basaltic lavas in the Westfiords (Iceland), which have never been intruded by dikes, contain no celadonite,

whereas celadonite is observed only within basaltic lavas hosting the dikes. All the examples above support the physicochemical model proposed in this study (Fig. 13).

Consequently, our model predicts celadonite in many volcanic environments due to the relative availability of the components required for celadonite precipitation. In addition, the interlayer sites of celadonite contain enough K and Rb contents to be used for age dating (e.g., Booij et al. 1995; Gallahan and Duncan 1994; Innocent et al. 1997; Laureijs et al. 2021). Therefore, a combination of specific source tracking, especially fluid sources, and age dating could provide other insights hidden in lower temperature regimes in volcanic and geothermal history.

ACKNOWLEDGMENTS

We thank Leslie L. Baker of the University of Idaho (USA) and Chang Oh Choo of the Andong National University (Korea) for providing constructive comments to improve the early version of manuscript. We are grateful to Dong-Yoon Lee, Woo-Yeol Kim, and Eun-Yeong Kang for helping filed works. Sehyeon Gwon and Soyoung Min are also thanked for discussions and encouragement. Thoughtful reviews from Douglas McCarty and an anonymous reviewer, and dedicated editorial handling from Warren D. Huff, led to significant improvements in this work.

FUNDING

This research was supported by the Basic Science Research Program through the National Research Foundation of Korea (NRF) funded by the Ministry of Education (2016R1A6A1A05011910).

REFERENCES CITED

Alt, J.C., Laverne, C., Coggon, R.M., Teagle, D.A.H., Banerjee, N.R., Morgan, S., Smith-Duque, C.E., Harris, M., and Galli, L. (2010) Subsurface structure of a submarine hydrothermal system in ocean crust formed at the East Pacific Rise, ODP/IODP Site 1256. Geochemistry, Geophysics, Geosystems, 11.

Alt, J.C., and Teagle, D.A.H. (2003) Hydrothermal alteration of upper oceanic crust formed at a fast-spreading ridge: mineral, chemical, and isotopic evidence from ODP Site 801. Chemical Geology, 201, 191–211.

Andrews, A.J. (1980) Saponite and celadonite in layer 2 basalts, DSDP Leg 37. Contributions to Mineralogy and Petrology, 73, 323–340.

Baker, L.L., Rember, W.C., Sprenke, K.F., and Strawn, D.G. (2012) Celadonite in continental flood basalts of the Columbia River Basalt Group. American Mineralogist, 97, 1284–1290.

Barzoi, S.C., and Seclaman, M. (2010) Petrographic and geochemical interpretation of the Late Cretaceous volcaniclastic deposits from the Hateg Basin. Palaeogeography, Palaeoclimatology, Palaeoecology, 293, 306–318.

Bau, M. (1996) Controls on the fractionation of isovalent trace elements in magmatic and aqueous systems: evidence from Y/Ho, Zr/Hf, and lanthanide tetrad effect. Contributions to Mineralogy and Petrology, 123, 323–333.

Böhlke, J.K., Alt, J.C., and Muehlenbachs, K. (1984) Oxygen isotope–water relations in altered deep-sea basalts: low-temperature mineralogical controls. Canadian Journal of Earth Sciences, 21, 67–77.

Booij, E., Gallahan ,W.E., and Staudigel, H. (1995) Ion-exchange experiments and Rb/Sr dating

on celadonites from the Troodos ophiolite, Cyprus. Chemical Geology, 126, 155–167.

Buckley, H.A., Bevan, J.C., Brown, K.M., Johnson, L.R., and Farmer, V.C. (1978) Glauconite and celadonite: two separate mineral species. Mineralogical Magazine, 42, 373–382.

Bustillo, M.A., and Martınez-Frıas, J. (2003) Green opals in hydrothermalized basalts (Tenerife Island, Spain): alteration and aging of silica pseudoglass. Journal of Non-Crystalline Solids, 323, 27–33.

Cathelineau, M., and Izquierdo, G. (1988) Temperature-composition relationships of authigenic micaceous minerals in the Los Azufres geothermal system. Contributions to Mineralogy and Petrology, 100, 418–428.

Choi, H.O., Choi, S.H., Lee, D.C., and Kang, H.C. (2013) Geochemical evolution of basaltic volcanism within the tertiary basins of southeastern Korea and the opening of the East Sea (Sea of Japan). Journal of Volcanology and Geothermal Research, 249, 109–122.

Clayton, R.N., O'Neil, J.R., and Mayeda, T.K. (1972) Oxygen isotope exchange between quartz and water. Journal of Geophysical Research, 77, 3057–3067.

Cummings, M.L., Trone, P.M., and Pollock, J.M. (1989) Geochemistry of colloidal silica precipitates in altered Grande Ronde Basalt, northeastern Oregon, USA. Chemical Geology, 75, 61–79.

Drits, V.A., Zviagina, B.B., McCarty, D.K., and Salyn, A.L. (2010) Factors responsible for crystal-chemical variations in the solid solutions from illite to aluminoceladonite and from glauconite to celadonite. American Mineralogist, 95, 348–361.

Dudoignon, P., Meunier, A., Beaufort, D., Gachon, A., and Buigues, D. (1989) Hydrothermal alteration at Mururoa Atoll (French Polynesia). Chemical Geology, 76, 385–401.

Eiler, J.M., Schiano, P., Kitchen, N., and Stolper, E.M. (2000) Oxygen-isotope evidence for recycled crust in the sources of mid-ocean-ridge basalts. Nature, 403, 530–534.

Gallahan, W.E., and Duncan, R.A. (1994) Spatial and temporal variability in crystallization of celadonites within the Troodos ophiolite, Cyprus: Implications for low-temperature alteration of the oceanic crust. Journal of Geophysical Research:Solid Earth, 99, 3147–3161.

Gilg, H.A., Morteani, G., Kostitsyn, Y., Preinfalk, C., Gatter, I., and Strieder, A.J. (2003) Genesis of amethyst geodes in basaltic rocks of the Serra Geral Formation (Ametista do Sul, Rio Grande do Sul, Brazil): a fluid inclusion, REE, oxygen, carbon, and Sr isotope study on basalt, quartz, and calcite. Mineralium Deposita, 38, 1009–1025.

Hajash, A. (1984) Rare earth element abundances and distribution patterns in hydrothermally altered basalts: experimental results. Contributions to Mineralogy and Petrology, 85, 409–412.

Herdianita, N.R., Browne, P.R.L., Rodgers, K.A., and Campbell, K.A. (2000) Mineralogical and textural changes accompanying ageing of silica sinter. Mineralium deposita, 35, 48–62.

Holland, T.J.B., and Redfern, S.A.T. (1997) Unit cell refinement from powder diffraction data; the use of regression diagnostics. Mineralogical Magazine, 61, 65–77.

Innocent, C., Parron, C., and Hamelin, B. (1997) Rb/Sr chronology and crystal chemistry of celadonites from the Paraná continental tholeiites, Brazil. Geochimca et Cosmochimica Acta, 61, 3753–3761.

Irvine, T.N.J., and Baragar, W.R.A. (1971) A guide to the chemical classification of the common volcanic rocks. Canadian Journal of Earth Sciences, 8, 523–548.

Jébrak, M. (1997) Hydrothermal breccias in vein-type ore deposits: a review of mechanisms, morphology and size distribution. Ore Geology Review, 12, 111–134.

Keeling, J.L., Zwingmann, H., Raven, M.D., and Self, P.G. (2018) Atypical alteration of biotite to celadonite and nontronite, southern Eyre Peninsula: timing and environmental factors. Proceedings for the 5th Australian Regolith Geoscientists Association Conference, Wallaroo, South Australia, 45–48.

Khim, B.K., Woo, K.S., and Sohn, Y.K. (2007) Distinct sedimentary processes reflected in the isotopic signatures of dolomitic concretions in the Miocene Pohang Basin (southwestern East Sea). Journal of Asian Earth Sciences, 29, 939–946.

Kim, M.C., Kim, J.S., Jung, S., Son, M., and Sohn, Y.K. (2011) Bimodal volcanism and classification of the Miocene basin fill in the northern area of the Janggi-myeon, Pohang, southeast Korea. Journal of the Geological Society of Korea, 47, 585–612 (in Korean with English abstract).

Laureijs, C.T., Coogan, L.A., and Spence, J. (2021) Regionally variable timing and duration of celadonite formation in the Troodos lavas (Cyprus) from Rb-Sr age distributions. Chemical Geology, 560, 119995.

Laverne, C., Grauby, O., Alt, J.C., and Bohn, M. (2006) Hydroschorlomite in altered basalts from Hole 1256D, ODP Leg 206: The transition from low-temperature to hydrothermal alteration. Geochemistry, Geophysics, Geosystems, 7.

Lepore, G.O., Bindi, L., Di Benedetto, F., Mugnaioli, E., Viti, C., Zanetti, A., Ciriotti, M.E., and Bonazzi, P. (2017) A multimethodic approach for the characterization of manganiceladonite, a new member of the celadonite family from Cerchiara mine, Eastern Liguria, Italy. Mineralogical Magazine, 81, 167–173.

Li, G., Peacor, D.R., Coombs, D.S., and Kawachi, Y. (1997) Solid solution in the celadonite family:

The new minerals ferroceladonite, $K_2Fe^{2+}_2Fe^{3+}_3Si_8O_{20}(OH)_4$, and ferroaluminoceladonite, $K_2Fe^{2+}_2Al_2Si_8O_{20}(OH)_4$. American Mineralogist, 82, 503–511.

Marescotti, P., Vanko, D.A., and Cabella, R. (2000) From oxidizing to reducing alteration: Mineralogical variations in pillow basalts from the east flank, Juan de Fuca Ridge. Proceedings of the Ocean Drilling Program, Scientific Results. 168, 119–136.

Meunier, A., Mas, A., Beaufort, D., Patrier, P., and Dudoignon, P. (2008) Clay minerals in basalt-hawaiite rocks from Mururoa atoll (French Polynesia). II. Petrography and geochemistry. Clays and Clay Minerals, 56, 730–750.

Miller, K.G., Wright, J.D., and Fairbanks, R.G. (1991) Unlocking the ice house: Oligocene-Miocene oxygen isotopes, eustasy, and margin erosion. Journal of Geophysical Research:Solid Earth, 96, 6829–6848.

Montanaro, C., Cronin, S., Scheu, B., Kennedy, B., and Scott, B. (2020) Complex crater fields formed by steam-driven eruptions: Lake Okaro, New Zealand. Geological Society of America Bulletin, 132, 1914–1930.

Moore, D.M., and Reynolds Jr, R.C. (1989) X-ray Diffraction and the Identification and Analysis of Clay Minerals. Oxford University Press.

Moraes, L.C.D., and Seer, H.J. (2018) Pillow lavas and fluvio-lacustrine deposits in the northeast of Paraná Continental Magmatic Province, Brazil. Journal of Volcanology and Geothermal Research, 355, 78–86.

Morteani, G., Kostitsyn, Y., Preinfalk, C., and Gilg, H.A. (2010) The genesis of the amethyst geodes at Artigas (Uruguay) and the paleohydrology of the Guaraní aquifer: structural, geochemical, oxygen, carbon, strontium isotope and fluid inclusion study. International Journal

of Earth Sciences, 99, 927–947.

Mosser-Ruck, R., Devineau, K., Charpentier, D., and Cathelineau, M. (2005) Effects of ethylene glycol saturation protocols on XRD patterns: a critical review and discussion. Clays and Clay Minerals, 53, 631–638.

Muller, F., Drits, V., Plançon, A., and Robert, J.L. (2000) Structural transformation of 2:1 dioctahedral layer silicates during dehydroxylation-rehydroxylation reactions. Clays and Clay Minerals, 48, 572–585.

Noh, J.H., and Boles, J.R. (1989) Diagenetic alteration of perlite in the Guryongpo area, Republic of Korea. Clays and Clay Minerals, 37, 47–58.

Noh, J.H., and Hong, J.S. (2005) Occurrence and genesis of perlite from the Beomgockri Group in Janggi area. Journal of Mineralogical Society of Korea, 18, 277–288 (in Korean with English abstract).

Odin, G.S., Desprairies, A., Fullagar, P.D., Bellon, H., Decarreau, A., Frohlich, F., and Zelvelder, M. (1988) Nature and geological significance of celadonite. In G.S. Odin, Ed., Developments in Sedimentology, 337–398. Elsevier, Amsterdam.

Ou, S. (2019) Hydrochemistry and isotope studies for circulation analysis of water in liquefaction zone in Pohang, 39 p. MSc thesis, University of Deajeon, Korea.

Pałgan, D., Devey, C.W., and Yeo, I.A. (2016) Dike control of hydrothermal circulation in the Tertiary Icelandic crust and implications for cooling of the seafloor. Journal of Volcanology and Geothermal Research, 316, 22–33.

Park, J.H., Kim, C.S., Kim, J.S., Sung, J.G., Kim, I.S., Lee, J.D., and Paik, I.S. (1999) Petrological study on the intermediate to mafic lavas distributed in Janggi area (1): general geology and

petrochemical characteristics. Journal of Petrological Society of Korea, 8, 149–170 (in Korean with English abstract).

Porter, S., Vanko, D.A., and Ghazi, A.M. (2000) Major and trace element compositions of secondary clays in basalts altered at low temperature, eastern flank of the Juan de Fuca Ridge. Proceedings of the Ocean Drilling Program, Scientific Results. 168, 149–157.

Renac, C., Kyser, K., Bowden, P., Moine, B., Cottin, J.Y. (2010) Hydrothermal fluid interaction in basaltic lava units, Kerguelen Archipelago (SW Indian Ocean). European Journal of Mineralogy, 22, 215–234.

Reolid, M., and Abad, I. (2014) Glauconitic laminated crusts from hydrothermal alteration of Jurassic pillow-lavas (Betic Cordillera, S Spain): a microbial influence case. Journal of Iberian Geology, 40, 389–408.

Rieder, M., Cavazzini, G., Dyakonov, Y.S., Frank-Kamenetskii, V.A., Gottardi, G., Guggenheim, S., Koval, P.V., Muller, G., Neiva, A.M.R., Radoslovich, E.W., and others. (1998) Nomenclature of the micas. Canadian Mineralogist, 36, 905–912.

Ring, U., and Pantazides, H. (2019) The uplift of the Troodos massif, Cyprus. Tectonics, 38, 3124–3139.

Rodríguez-Losada, J.A., Martinez-Frias, J., Bustillo, M.A., Delgado, A., Hernandez-Pacheco, A., and de la Fuente Krauss, J.V. (2000) The hydrothermally altered ankaramite basalts of Punta Poyata (Tenerife, Canary Islands). Journal of Volcanology and Geothermal Research, 103, 367–376.

Rollinson, H.R. (2014) Using Geochemical Data: Evaluation, Presentation, Interpretation. Routledge, London.

Schenato, F., Formoso, M.L.L., Dudoignon, P., Meunier, A., Proust, D., and Mas, A. (2003) Alteration processes of a thick basaltic lava flow of the Paraná Basin (Brazil): petrographic and mineralogical studies. Journal of South American Earth Sciences, 16, 423–444.

Schramm, B., Devey, C.W., Gillis, K.M., and Lackschewitz, K. (2005) Quantitative assessment of chemical and mineralogical changes due to progressive low-temperature alteration of East Pacific Rise basalts from 0 to 9 Ma. Chemical Geology, 218, 281–313.

Sheppard, S.M.F., and Gilg, H.A. (1996) Stable isotope geochemistry of clay minerals. Clay Minerals, 31, 1–24.

Shim, S.H., Park, B.J., Kim, T H., Jang, Y.D., Kim, J.H., and Kim, J.J. (2011) Petrology of the Tertiary basaltic rocks in the Yeonil and Eoil Basins, southeastern Korea. Journal of Petrological Society of Korea, 20, 1–21 (in Korean with English abstract).

Shin, S.C. (2013) Revised fission-track ages and chronostratigraphies of the Miocene basin-fill volcanics and basements, SE Korea. Journal of Petrological Society of Korea, 22, 83–115 (in Korean with English abstract).

Skilling, I.P., White, J.D., and McPhie, J. (2002) Peperite: a review of magma–sediment mingling. Journal of Volcanology and Geothermal Research, 114, 1–17.

Sohn, Y.K., Ki, J.S., Jung, S., Kim, M.C., Cho, H., and Son, M. (2013) Synvolcanic and syntectonic sedimentation of the mixed volcaniclastic–epiclastic succession in the Miocene Janggi Basin, SE Korea. Sedimentary Geology, 288, 40–59.

Son, M., Song, C.W., Kim, M.C., Cheon, Y., Cho, H., and Sohn, Y.K. (2015) Miocene tectonic evolution of the basins and fault systems, SE Korea: dextral, simple shear during the East Sea (Sea of Japan) opening. Journal of the Geological Society, 172, 664–680.

Talbi, E.H., and Honnorez, J. (2003) Low-temperature alteration of Mesozoic oceanic crust, Ocean Drilling Program Leg 185. Geochemistry, Geophysics, Geosystems, 4.

Teagle, D.A.H., Alt, J.C., Bach, W., Halliday, A.N., and Erzinger, J. (1996) Alteration of upper ocean crust in a ridge-flank hydrothermal upflow zone: mineral, chemical, and isotopic constraints from Hole 896A. Proceedings of the Ocean Drilling Program, Scientific Results. 148, 119–150.

Tischendorf, G., Forster, H.J., Gottesmann, B., and Rieder, M. (2007) True and brittle micas: composition and solid-solution series. Mineralogical Magazine, 71, 285–320.

Tóth, E., Weiszburg, T.G., Jeffries, T., Williams, C.T., Bartha, A., Bertalan, É., and Cora, I. (2010) Submicroscopic accessory minerals overprinting clay mineral REE patterns (celadonite–glauconite group examples). Chemical Geology, 269, 312–328.

Velde, B. (1972) Celadonite mica: solid solution and stability. Contributions to Mineralogy and Petrology, 37, 235–247.

Verberne, B.A., Plümper, O., and Spiers, C.J. (2019) Nanocrystalline principal slip zones and their role in controlling crustal fault rheology. Minerals, 9, 328.

Whitney, D.L., and Evans, B.W. (2010) Abbreviations for names of rock-forming minerals. American Mineralogist, 95, 185–187.

Wise, W.S., and Eugster, H.P. (1964) Celadonite: synthesis, thermal stability and occurrence. American Mineralogist, 49, 1031–1083.

Wood, D.A., Gibson, I.L., and Thompson, R.N. (1976) Elemental mobility during zeolite facies metamorphism of the Tertiary basalts of eastern Iceland. Contributions to Mineralogy and Petrology, 55, 241–254.

Zhang, L.G., Liu, J.X., Zhou, H.B., and Chen, Z.S. (1989) Oxygen isotope fractionation in the quartz-water-salt system. Economic Geology, 89, 1643–1650.

FIGURE CAPTIONS

Figure 1. Geological outline of the study area. (a) Distribution of the Miocene basins in the southeastern Korean Peninsula. (b) Geological map of the study area.

Figure 2. Occurrence and petrography of dacitic–rhyolitic lapilli tuff and basaltic volcanics. (a) A representative outcrop (zeolite quarry) of dacitic–rhyolitic lapilli tuff interlayered with lacustrine tuffaceous sediments. (b) Dacitic–rhyolitic lapilli tuff under plane polarized light (PPL). (c) Lithological boundary between basaltic tuff breccia and trachytic basalt. (d) Trachytic basalt with typical flow joints. Refer to stereonet (left inset) for the orientation of the flow joints around the study area. (e) Trachytic basalt under cross polarized light (XPL). A trachytic texture is shown in the left inset. (f) Lithological boundary between trachytic and porphyritic basalts. (g) Porphyritic basalt under XPL. The plagioclase phenocryst (right) is ~5 mm. (h–i) A representative outcrop and XPL image, respectively, of the microcrystalline basalt.

Figure 3. The occurrence of celadonite. (a) A representative outcrop of fault-filling earthy celadonite. The right inset shows the orientations of celadonite deposits (n = 49; roughly E-W trending) in the study area. The fragments of trachytic basalt have mosaic fabric, indicating fault brecciation. (b) Fault-filling earthy celadonite with a relatively small amount of trachytic basalt fragments. (c) A representative outcrop of fracture-filling vitreous celadonite. (d) A Carbonate

(calcite) vein, where fault-filling vitreous celadonite contacts the trachytic basalt host. (e) A quartz vein grading into the vitreous celadonite.

Figure 4. XRD results from the samples (See also Table 2 for further details). The reference peaks for celadonite are from Baker et al. (2012), Buckley et al. (1978), Li et al. (1997), and Odin et al. (1988). The opal-A peak band (at 16–32 2θ° in CELA-2 and -3 samples) resembling that of the green opal of Bustillo and Martinez-Frias (2003) is observed in the CELA-2 and CELA-3 samples. The differences from 100% may represent minor smectite. The peak overlapping with quartz at ~20.5 and ~26.5 2θ° may produce some phase underestimation or overestimation.

Figure 5. Petrography of celadonite. (a–b) A representative celadonite vein containing reddish altered trachytic basalt and mineral fragments under PPL and XPL, respectively. (c–d) Celadonite injected into trachytic basalt fragments and minerals. (e) and (f) are the back scattered electron (BSE) images of (c) and (d), respectively. The alteration of phenocrysts within basalt fragments is insignificant, but the mesostasis of basaltic fragments is strongly altered.

Figure 6. Major element variations in volcanics and celadonite. (a) TAS diagram and (b–e) Harker diagrams for the volcanics distributed in the study area. The alkaline versus sub-alkaline boundary is based on Irvine and Baragar (1971). The published data for volcanics are from Choi et al. (2013), Kim et al. (2011), Noh and Hong (2005), Park et al. (1999), and Shim et al. (2011), and for celadonite and celadonite-opal mixture (i.e., green opal) from Odin et al. (1988) and Bustillo and

Martinez-Frias (2003), respectively. All data are provided in ESM 1 and 3. The compositions of the mesostasis in basaltic lavas were obtained during EMP analysis in this study (ESM 2).

Figure 7. Chondrite-normalized trace element patterns for (a) the basaltic and dacitic-rhyolitic volcanics, and (b) the celadonite. The modeled celadonite (i.e., {(CELA-1 + CELA-2) / 2} * 3) shows a pattern similar to the basaltic volcanics. Data for the C1-chondrite, Mid-Ocean Ridge Basalts (MORB), and Post-Archean Australian average Sedimentary (PAAS) are from Rollinson (2014). The published data for volcanics are from Choi et al. (2013), Kim et al. (2011), Park et al. (1999), and Shim et al. (2011). The REEs contents of the Hungarian celadonite are from Tóth et al. (2010). See ESM 1 and 3 for the published data.

Figure 8. The $\delta^{18}O_{V\text{-}SMOW}$ comparison. Oxygen isotope ratios for the global celadonite (ESM 3) are from Alt et al. (2010), Alt and Teagle (2003), Böhlke et al. (1984), Odin et al. (1988), and Renac et al. (2010), MORBs are from Eiler et al. (2000), the Middle Miocene seawater are from Miller et al. (1991), the carbonate concretions in the Middle Miocene marine Pohang Basin (Fig. 1a) are from Khim et al. (2007), and the present sea and groundwater are from Ou (2019).

Figure 9. BSE images and accompanying EMP analytical points (crosses) for (a–c) pyroxene phenocrysts, microlites, mesostasis, and (d) celadonite. The differences between the fresh basalts (a and c) and altered basalt (b) are remarkable. The co-precipitation of celadonite and opal suggests an equilibrium state.

Figure 10. (a) Celadonite classification after Li et al. (1997) and Tischendorf et al. (2007); *mgil* = Mg - Li, *feal* = $^{VI}Fe_{total}$ + Mn + Ti - ^{VI}Al, both are in atoms per formula unit (apfu) (See also ESM 4). (b) K_2O versus SiO_2 diagram for celadonite. Most of celadonites from the other cases are mixed with smectites, whereas the celadonite in this study is mixed with opal.

Figure 11. Oxygen isotope extrapolation from the celadonite-opal mixing trend (See also Table 3 for further details).

Figure 12. Oxygen isotope thermometric fractionation curve (ESM 3) for tracking fluid composition precipitating celadonite and opal. The fluid candidates mixing models are represented along the abscissa. The oxygen isotope compositions of fluid end-members are provided in ESM 3.

Figure 13. (a) Schematic illustration of the celadonite-forming process. (b) The micro–nanoparticles exhibit gradational oxidation with respect to their size. The scanning electron image shows a snapshot of the celadonite being formed by oxidation of smectite by opal.

This is the peer-reviewed, final accepted version for American Mineralogist, published by the Mineralogical Society of America.
The published version is subject to change. Cite as Authors (Year) Title. American Mineralogist, in press.
DOI: https://doi.org/10.2138/am-2022-8045. http://www.minsocam.org/

Table 1. The global occurrences of celadonite.

References	Location	Host rock	Main	T (°C)	Mechanism
Alt and Teagle (2003)	Leg 129 of ODP	Basaltic lava	Replacement of Ol Filling vesicles	34–67[a]	SWA[b]
Andrews (1980) Baker et al. (2012)	Leg 37 of DSDP Grande Ronde Basalt, U.S.A. Hateg Basin, Romania	Basaltic lava	Lining or filling of vesicles	<100	SWA
		Basaltic lava	Lining or filling of vesicles	15–35	GWA[c]
Barzoi and Seclaman (2010)		Andesitic fragments	Replacement of Px and Hbl Lining of filling of vesicles	-	SWA?
Böhlke et al. (1984)	Leg 51 of DSDP (Site 417A and D)	Basaltic lava	Replacement of Ol Filling of vesicles	14–26[a]	SWA
Booij et al. (1995); Gallahan and Duncan	Troodos Ophiolite, Cyprus	Basaltic lava	Lining or filling of vesicles or fractures	-	SWA

(1994)					
Cathelineau and Izquierdo (1988)	Los Azufres, Mexico	Andesitic lava	Replacement of Px	~240	-
Dudoignon et al. (1989)	Mururoa Atoll, France	Basaltic lava	Replacement of Ol and mesostasis	<100	SWA
Gilg et al. (2003)	Ametista do Sul, Brazil	Basaltic lava	Lining of vesicles	50–80	GWA
Innocent et al. (1997)	Parana Basin, Brazil	Basaltic lava	Lining or filling of vesicles or fractures	-	GWA
Keeling et al. (2018)	Uley mine and Sleaford Bay, Australia	Graphitic schist	Replacement of Bt	-	-
Laverne et al. (2006); Alt et al. (2010)	Leg 206 of IODP (Hole 1256D)	Basaltic lava	Replacement of Ol, Px, and Afs Filling of vesicles	~100 70–100[a]	SWA
Li et al.	Hokonui	Andesitic–	Replacement of	-	-

(1997)	Hills, New Zealand	rhyolitic tuff	shards Lining of vesicles		
Marescotti et al. (2000); Porter et al. (2000)	Leg 168 of IODP	Basaltic lava	Lining or filling of vesicles or fractures	<40	SWA
Moraes and Seer (2018)	Bauru Basin, Brazil	Basaltic lava	Filling of vesicles	-	Interaction with lacustrine sediments
Morteani et al. (2010)	Artigas, Uruguay	Basaltic–andesitic lava	Filling of vesicles Metasomatized Qz fragments	<120	GWA
Reolid and Abad (2014)	Betic Cordillera, Spain	Basaltic lava	Lining or filling of fractures	<100	Microbial activity
Renac et al. (2010)	Kerguelen Archipelago, France	Basaltic lava	Lining or filling of vesicles	180–205[a]	GWA

Rodríguez-Losada et al. (2000); Bustillo and Martinez-Frias (2003)	Tenerife Island, Spain	Basaltic lava	Lining of vesicles or fractures	-	SWA
Schenato et al. (2003)	Parana Basin, Brazil	Basaltic lava	Replacement of Ol Lining or filling of vesicles	-	Deuteric alteration
Schramm et al. (2005)	EXCO of the SE Pacific Rise	Basaltic lava	Replacement of Ol, Px, and Fe-$(OH)_x$ Lining or filling of vesicles	-	SWA
Talbi and Honnorez (2003)	Leg 185 of IODP	Basaltic lava	Replacement of Ol and mesostasis Filing of vesicles and fractures	<45	SWA

Tóth et al. (2010)	Úrkút Formation, Hungary	Mn-rich black shale	Thin laminations or flakes	-	Diagenesis

Notes: [a]Based on oxygen isotope thermometry, [b]Seawater alteration, [c]Groundwater alteration.

This is the peer-reviewed, final accepted version for American Mineralogist, published by the Mineralogical Society of America.
The published version is subject to change. Cite as Authors (Year) Title. American Mineralogist, in press.
DOI: https://doi.org/10.2138/am-2022-8045. http://www.minsocam.org/

Table 2. Powder XRD data and the associated (hkl) peaks and unit cell parameters.

(hkl)	CELA-1 (Å)	CELA-2 (Å)	CELA-3 (Å)	Ferroceladonite–Ferroaluminoceladonite[a] (Å)	Celadonite[b] (Å)
(001)	10.006	10.029	9.984	10.00	9.97
(020)	4.519	4.523	4.514	4.55	4.53
(11-1)	4.348	4.348	4.339	4.37	4.35
(021)	4.120	4.124	4.135	4.14	4.14
(11-2)	3.626	3.626	3.626	3.65	3.635
(022)	3.350	3.350	-	3.358	3.35
(003)	3.320	3.325	-	3.321	3.318
(112)	3.088	3.090	-	3.090	3.087
(11-3)	2.896	-	-	2.91	2.90
(023)	2.677	2.677	2.672	2.671	2.678
(130)	2.603	2.601	2.604	2.607	2.604
(13-1)	2.575	2.575	2.572	2.584	2.580
(13-2)	2.396	2.396	2.396	2.41	2.402
(13-3)	2.146	2.149	2.147	2.155	2.148
(006)	1.661	1.661	1.661	1.660	-
(33-1)	1.518	1.518	1.517	1.519	-
(060)	1.509	1.510	1.507	-	1.509
a	5.259(1)	5.258(1)	5.263(1)	5.270(5)	5.23(2)
b	9.057(1)	9.062(1)	9.055(1)	9.106(7)	9.06(1)
c	10.123(1)	10.126(2)	10.119(2)	10.125(8)	10.13(2)
β (°)	100.425(23)	100.425(27)	100.010(36)	100.27(14)	100.55(10)

Notes: [a]Li et al. (1997), [b]Wise and Eugster (1964), See also Drits et al. (2010) for comparison.

This is the peer-reviewed, final accepted version for American Mineralogist, published by the Mineralogical Society of America.
The published version is subject to change. Cite as Authors (Year) Title. American Mineralogist, in press.
DOI: https://doi.org/10.2138/am-2022-8045. http://www.minsocam.org/

Table 3. Estimation of the oxygen isotope compositions ($\delta^{18}O_{V\text{-}SMOW}$) for pure celadonite and opal.

	Pure celadonite ($\delta^{18}O_{V\text{-}SMOW}$)	Pure opal ($\delta^{18}O_{V\text{-}SMOW}$)	R^2
$\delta^{18}O$‰ vs. SiO_2 wt%	6.29	16.78	0.99
$\delta^{18}O$‰ vs. K_2O wt%[a]	7.62[a]	13.27[a]	0.12[a]
$\delta^{18}O$‰ vs. Cel_{XRD}%	9.02	14.37	0.76
$\delta^{18}O$‰ vs. Opl_{XRD}%	9.31	14.37	0.77
Average	8.21	15.18	

Notes: [a]Excepted for average due to its low correlation coefficient.

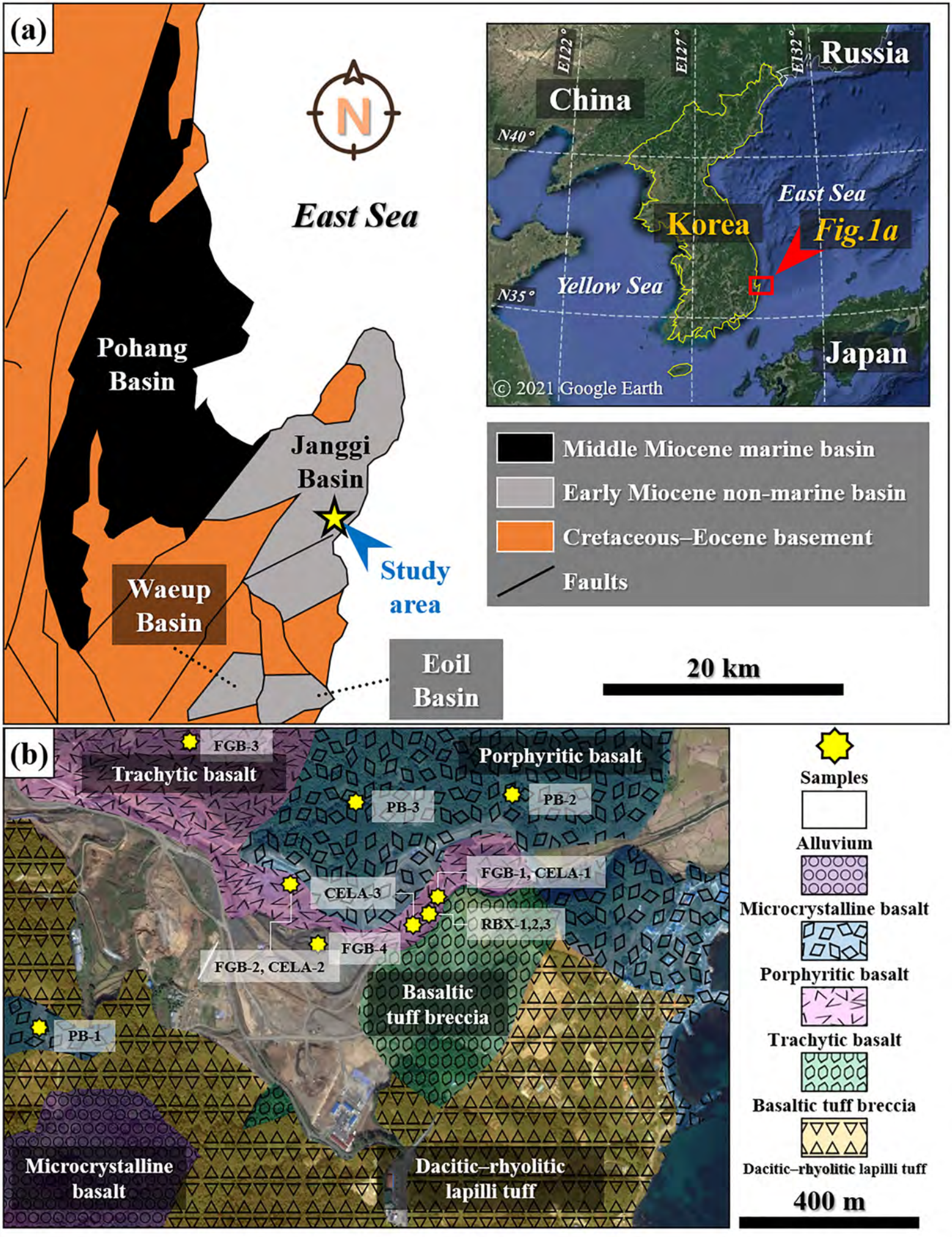
(a)
East Sea
Pohang Basin
Janggi Basin
Waeup Basin
Eoil Basin
Study area
20 km
Middle Miocene marine basin
Early Miocene non-marine basin
Cretaceous–Eocene basement
Faults
E122°
E127°
E132°
N40°
N35°
China
Russia
Korea
Japan
East Sea
Yellow Sea
Fig.1a
© 2021 Google Earth
(b)
FGB-3
Trachytic basalt
Porphyritic basalt
PB-3
PB-2
FGB-1, CELA-1
CELA-3
RBX-1,2,3
FGB-4
FGB-2, CELA-2
Basaltic tuff breccia
PB-1
Microcrystalline basalt
Dacitic–rhyolitic lapilli tuff
Samples
Alluvium
Microcrystalline basalt
Porphyritic basalt
Trachytic basalt
Basaltic tuff breccia
Dacitic–rhyolitic lapilli tuff
400 m

FIGURE 1

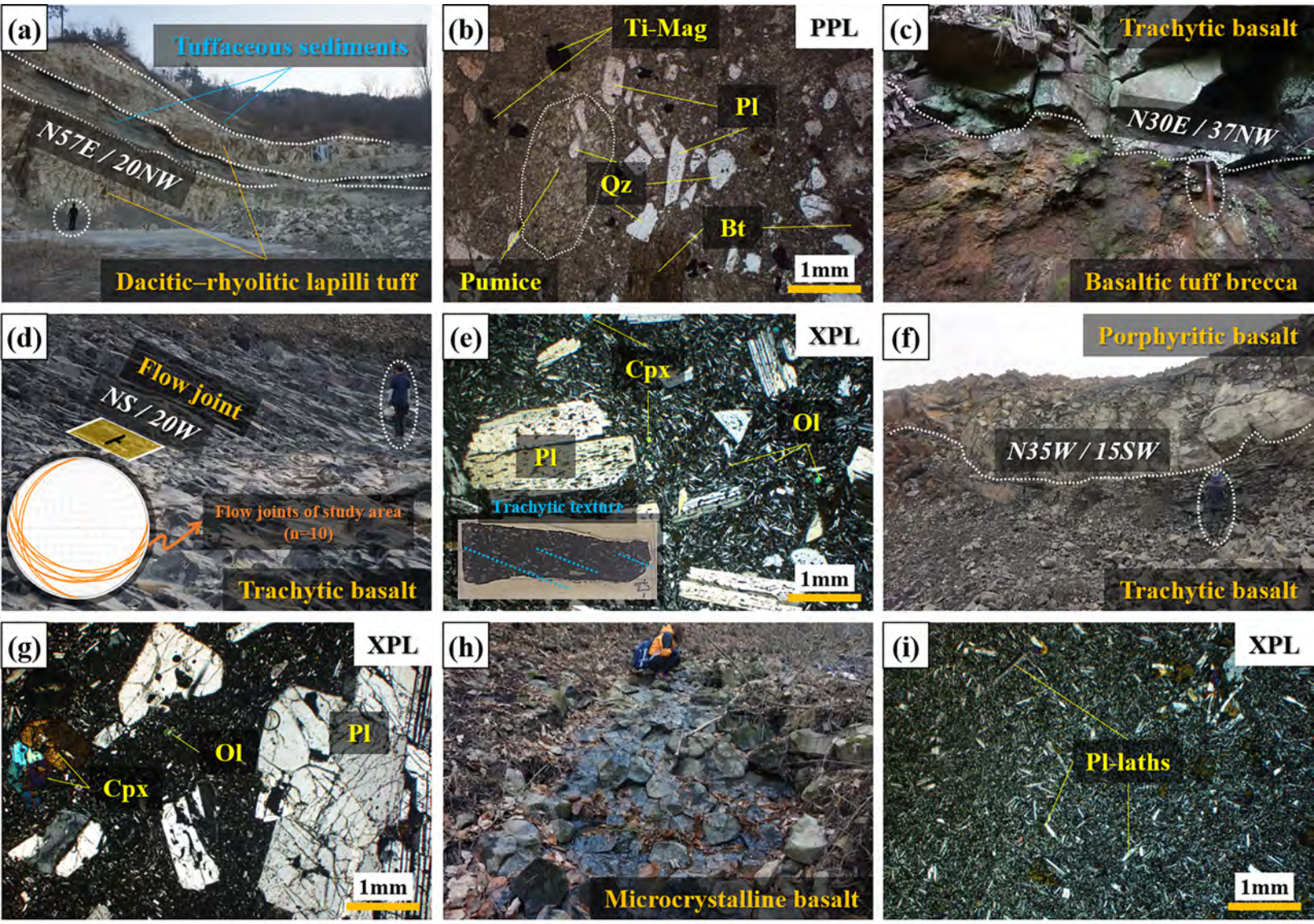
(a)
Tuffaceous sediments
N57E / 20NW
Dacitic–rhyolitic lapilli tuff
(b)
Ti-Mag
PPL
Pl
Qz
Bt
Pumice
1mm
(c)
Trachytic basalt
N30E / 37NW
Basaltic tuff brecca
(d)
Flow joint
NS / 20W
Flow joints of study area
(n=10)
Trachytic basalt
(e)
XPL
Cpx
Ol
Pl
Trachytic texture
1mm
(f)
Porphyritic basalt
N35W / 15SW
Trachytic basalt
(g)
XPL
Ol
Pl
Cpx
1mm
(h)
Microcrystalline basalt
(i)
XPL
Pl-laths
1mm

FIGURE 2

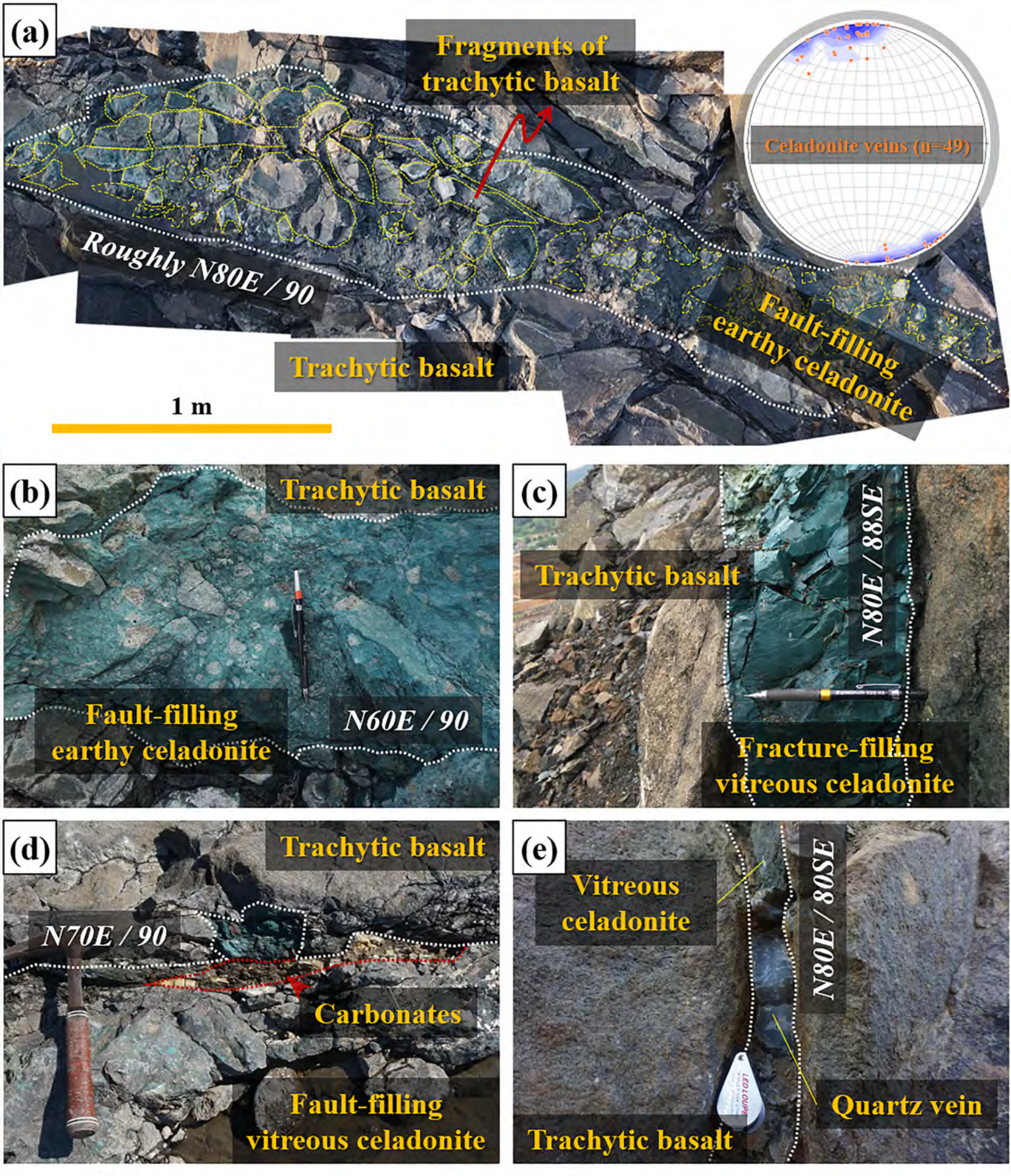
(a)
Fragments of trachytic basalt
Celadonite veins (n=49)
Roughly N80E / 90
Fault-filling earthy celadonite
Trachytic basalt
1 m
(b)
Trachytic basalt
Fault-filling earthy celadonite
N60E / 90
(c)
Trachytic basalt
N80E / 88SE
Fracture-filling vitreous celadonite
(d)
Trachytic basalt
N70E / 90
Carbonates
Fault-filling vitreous celadonite
(e)
Vitreous celadonite
N80E / 80SE
Quartz vein
Trachytic basalt

FIGURE 3

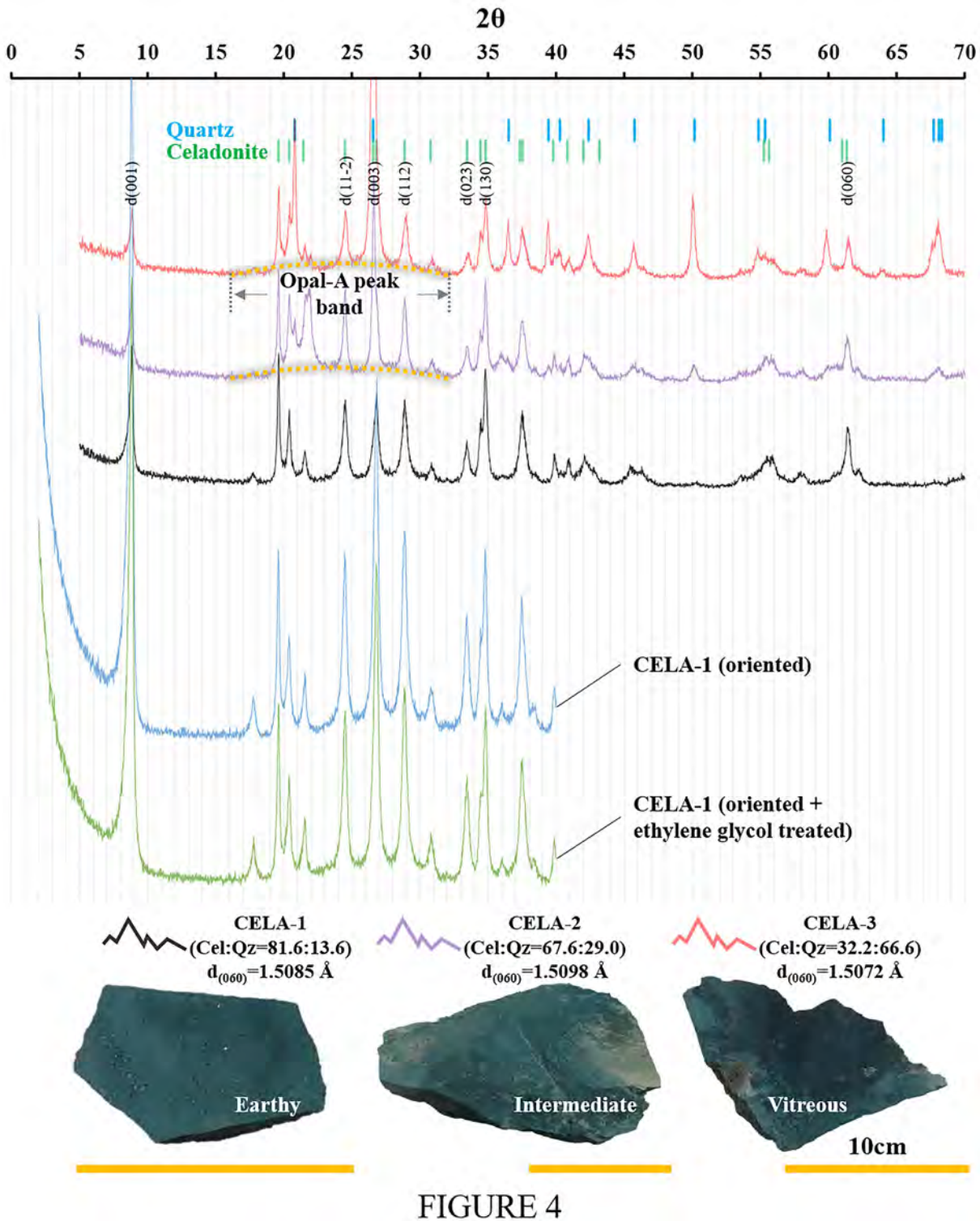
2θ
0
5
10
15
20
25
30
35
40
45
50
55
60
65
70
Quartz
Celadonite
d(001)
d(11-2)
d(003)
d(112)
d(023)
d(130)
d(060)
Opal-A peak band
CELA-1 (oriented)
CELA-1 (oriented + ethylene glycol treated)
CELA-1
(Cel:Qz=81.6:13.6)
d(060)=1.5085 Å
CELA-2
(Cel:Qz=67.6:29.0)
d(060)=1.5098 Å
CELA-3
(Cel:Qz=32.2:66.6)
d(060)=1.5072 Å
Earthy
Intermediate
Vitreous
10cm

FIGURE 4

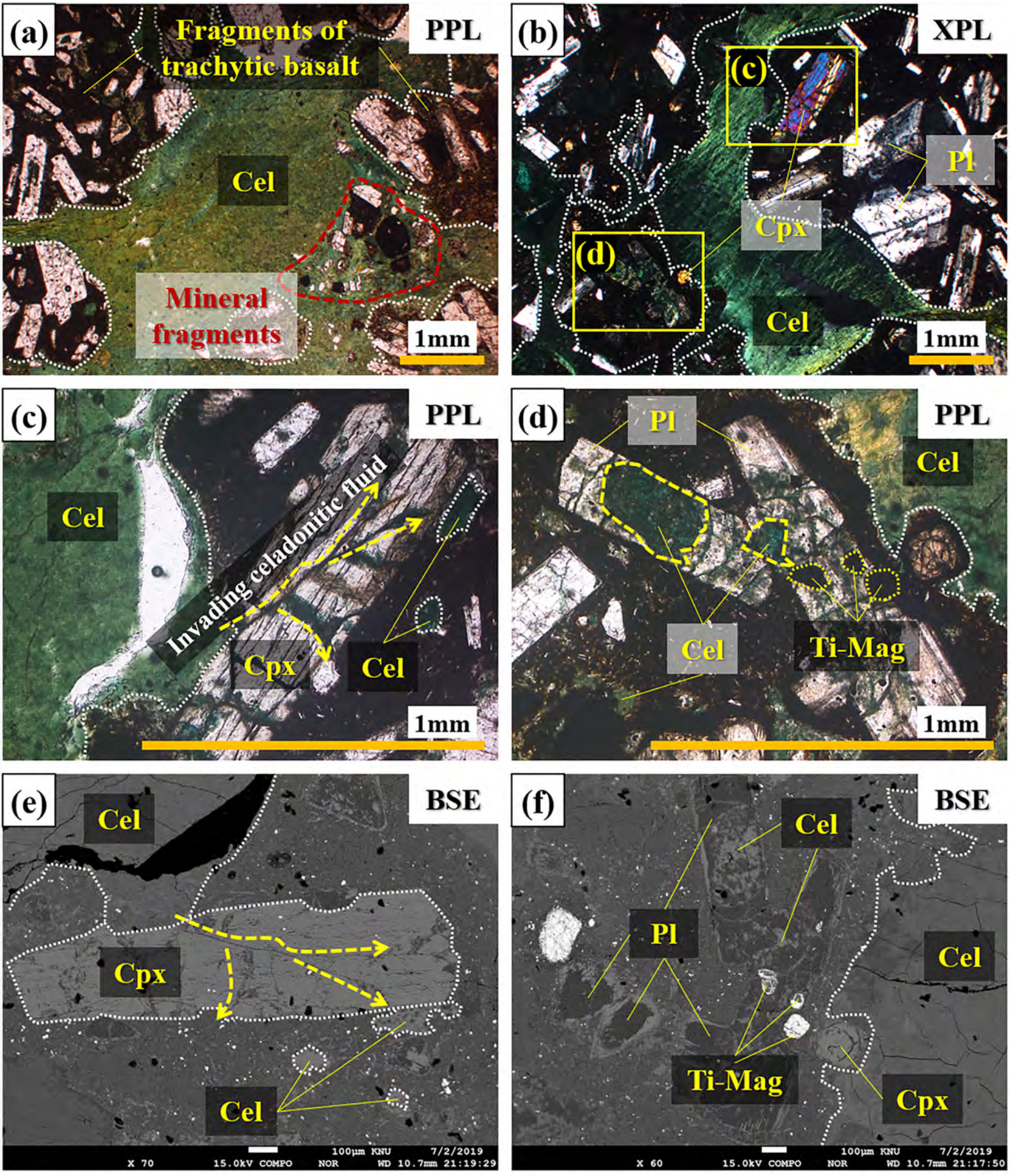
(a)
PPL
Fragments of trachytic basalt
Cel
Mineral fragments
1mm
(b)
XPL
(c)
Pl
Cpx
(d)
Cel
1mm
(c)
PPL
Cel
Invading celadonitic fluid
Cpx
Cel
1mm
(d)
PPL
Pl
Cel
Cel
Ti-Mag
1mm
(e)
BSE
Cel
Cpx
Cel
X 70
15.0kV COMPO
100μm KNU
NOR
7/2/2019
WD 10.7mm 21:19:29
(f)
BSE
Cel
Pl
Cel
Ti-Mag
Cpx
X 60
15.0kV COMPO
100μm KNU
NOR
7/2/2019
WD 10.7mm 21:17:50

FIGURE 5

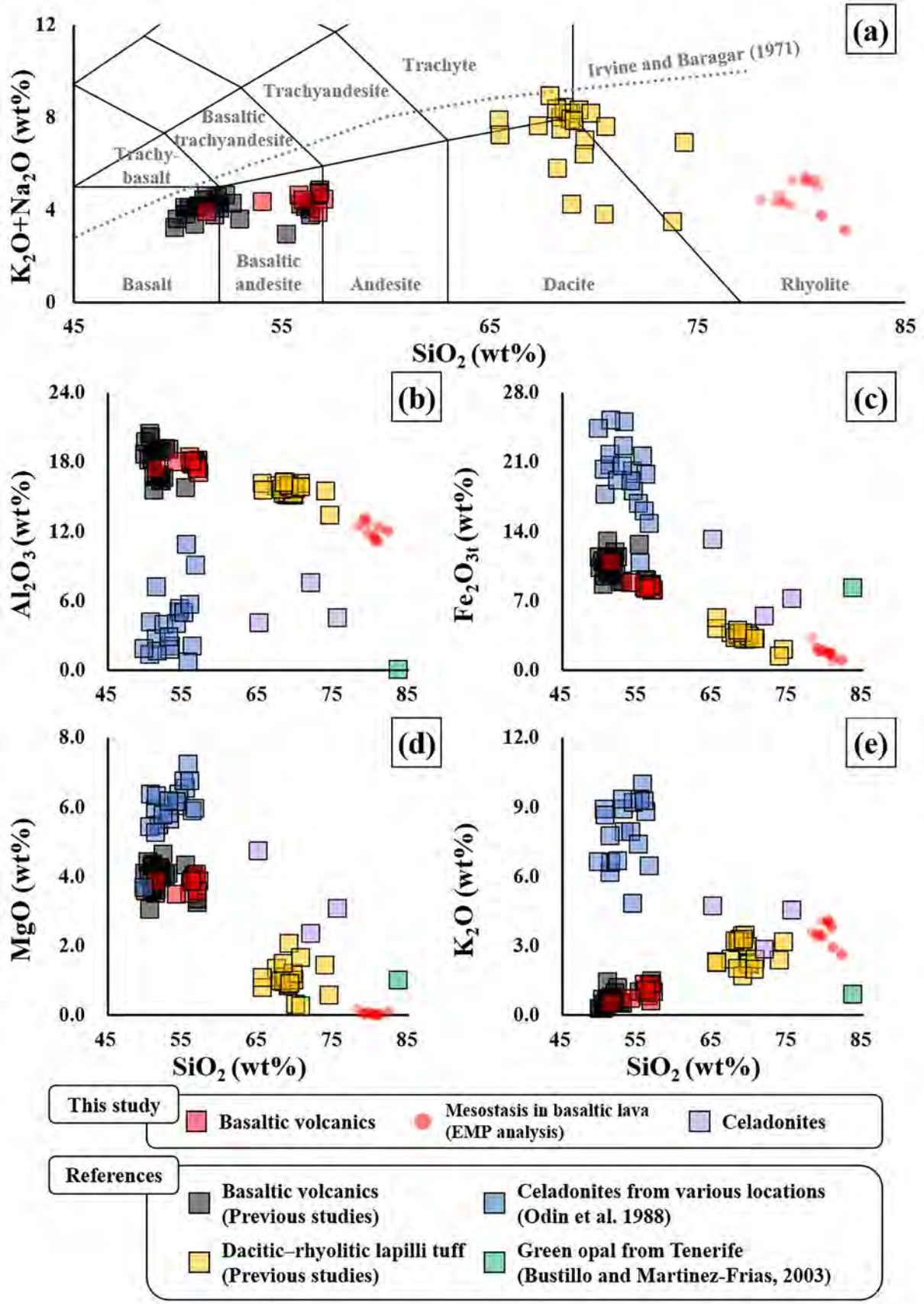
(a)
Trachyte
Irvine and Baragar (1971)
Trachyandesite
Basaltic trachyandesite
Trachy-basalt
Basalt
Basaltic andesite
Andesite
Dacite
Rhyolite
K2O+Na2O (wt%)
SiO2 (wt%)
(b)
Al2O3 (wt%)
(c)
Fe2O3t (wt%)
(d)
MgO (wt%)
(e)
K2O (wt%)
This study
Basaltic volcanics
Mesostasis in basaltic lava (EMP analysis)
Celadonites
References
Basaltic volcanics (Previous studies)
Celadonites from various locations (Odin et al. 1988)
Dacitic–rhyolitic lapilli tuff (Previous studies)
Green opal from Tenerife (Bustillo and Martinez-Frias, 2003)

FIGURE 6

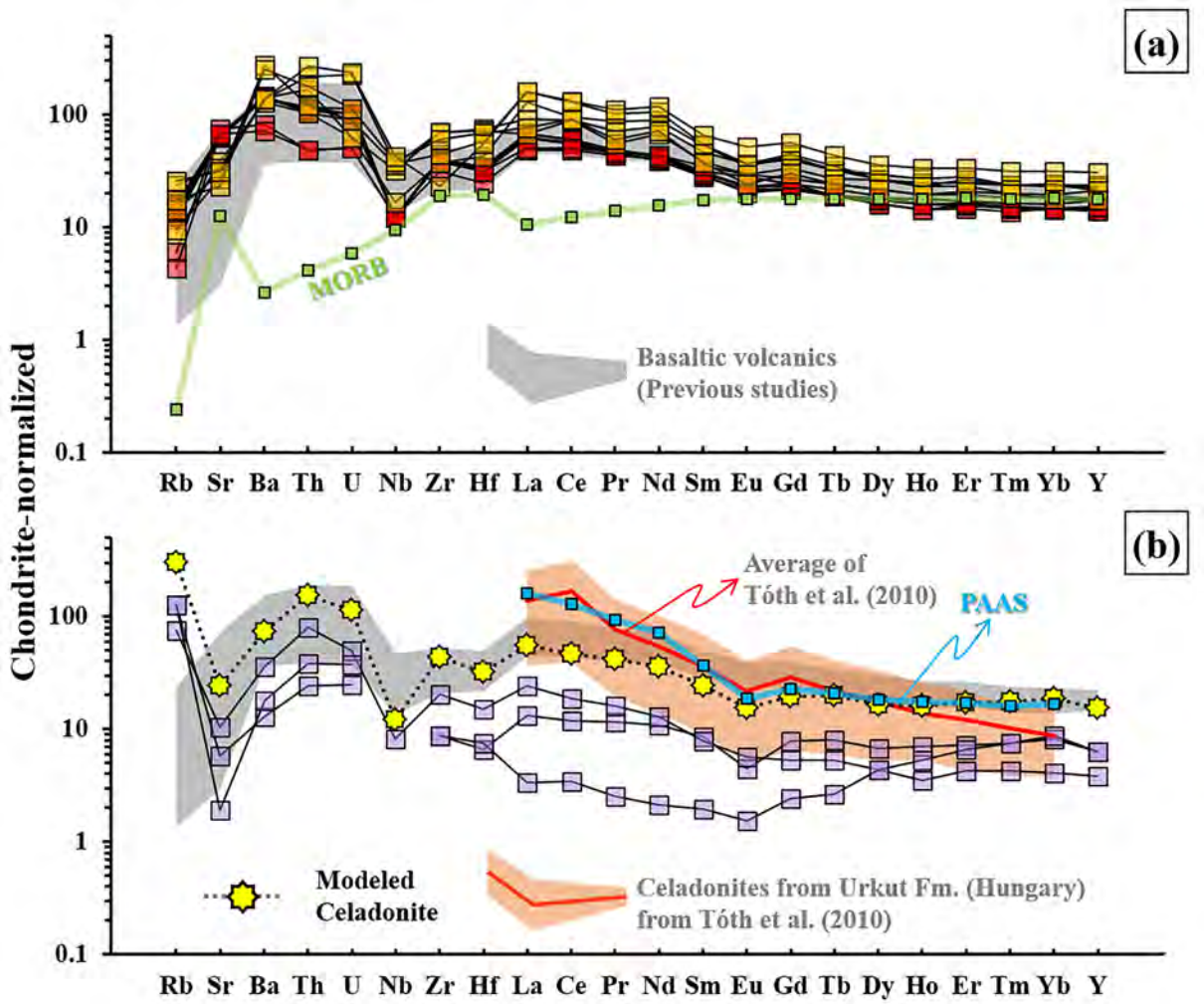
(a)
Chondrite-normalized
100
10
1
0.1
MORB
Basaltic volcanics
(Previous studies)
Rb Sr Ba Th U Nb Zr Hf La Ce Pr Nd Sm Eu Gd Tb Dy Ho Er Tm Yb Y
(b)
Average of
Tóth et al. (2010)
PAAS
Modeled
Celadonite
Celadonites from Urkut Fm. (Hungary)
from Tóth et al. (2010)
Rb Sr Ba Th U Nb Zr Hf La Ce Pr Nd Sm Eu Gd Tb Dy Ho Er Tm Yb Y

FIGURE 7

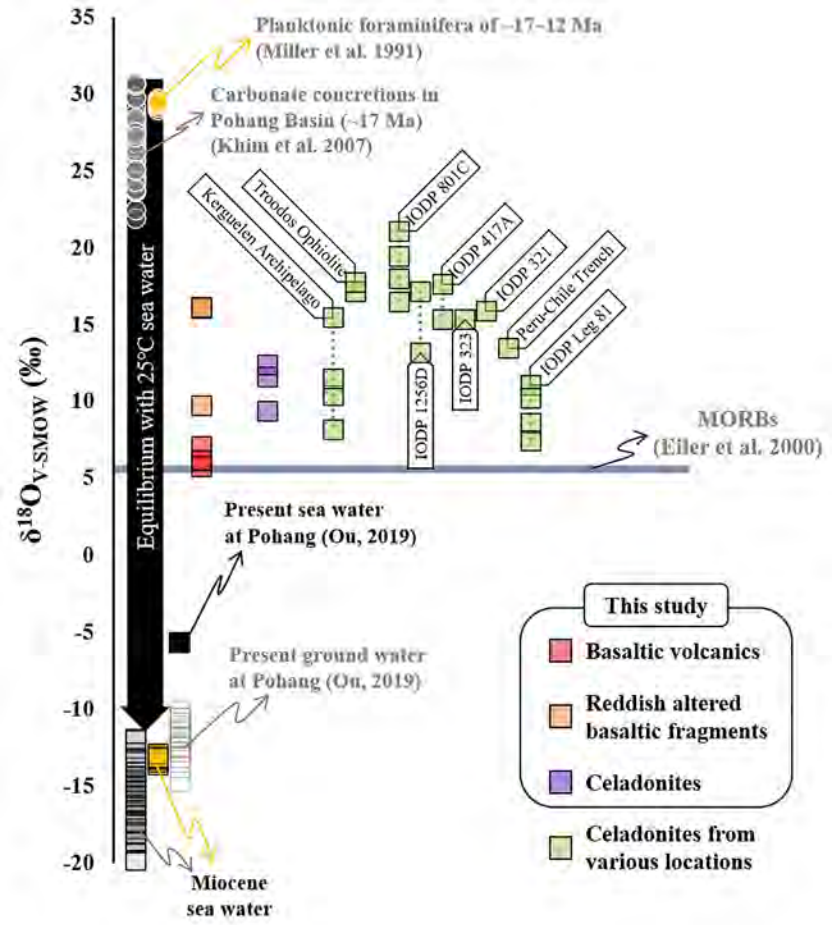
Planktonic foraminifera of ~17~12 Ma
(Miller et al. 1991)
Carbonate concretions in
Pohang Basin (~17 Ma)
(Khim et al. 2007)
Troodos Ophiolite
Kerguelen Archipelago
IODP 801C
IODP 417A
IODP 321
Peru-Chile Trench
IODP Leg 81
IODP 1256D
IODP 323
MORBs
(Eiler et al. 2000)
Equilibrium with 25°C sea water
Present sea water
at Pohang (Ou, 2019)
Present ground water
at Pohang (Ou, 2019)
Miocene
sea water
δ18OV-SMOW (‰)
35
30
25
20
15
10
5
0
-5
-10
-15
-20
This study
Basaltic volcanics
Reddish altered
basaltic fragments
Celadonites
Celadonites from
various locations

FIGURE 8

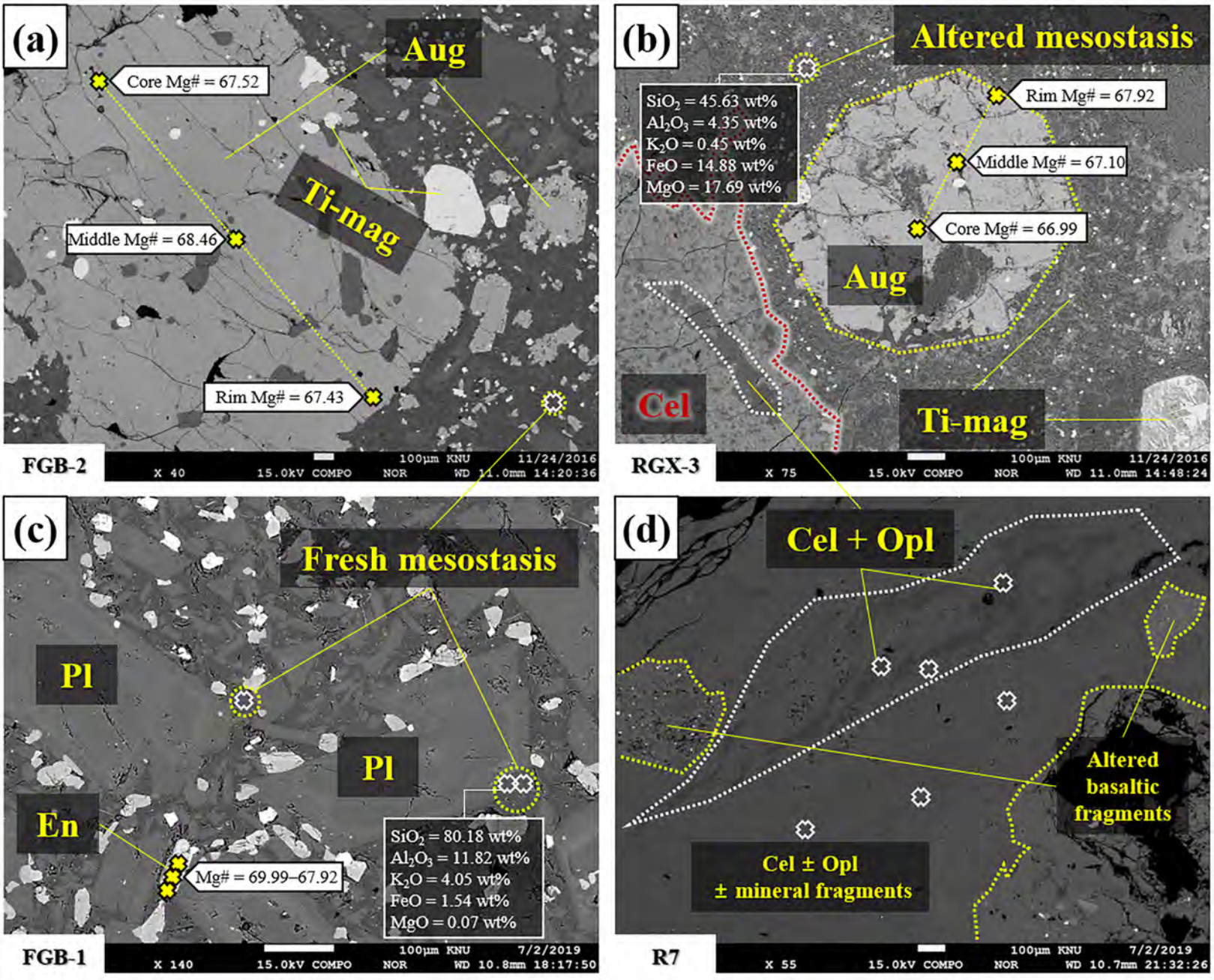
(a)
Aug
Core Mg# = 67.52
Ti-mag
Middle Mg# = 68.46
Rim Mg# = 67.43
FGB-2
X 40 15.0kV COMPO NOR WD 11.0mm 14:20:36
100μm KNU 11/24/2016
(b)
Altered mesostasis
SiO2 = 45.63 wt%
Al2O3 = 4.35 wt%
K2O = 0.45 wt%
FeO = 14.88 wt%
MgO = 17.69 wt%
Rim Mg# = 67.92
Middle Mg# = 67.10
Core Mg# = 66.99
Aug
Cel
Ti-mag
RGX-3
X 75 15.0kV COMPO NOR WD 11.0mm 14:48:24
100μm KNU 11/24/2016
(c)
Fresh mesostasis
Pl
Pl
En
Mg# = 69.99–67.92
SiO2 = 80.18 wt%
Al2O3 = 11.82 wt%
K2O = 4.05 wt%
FeO = 1.54 wt%
MgO = 0.07 wt%
FGB-1
X 140 15.0kV COMPO NOR WD 10.8mm 18:17:50
100μm KNU 7/2/2019
(d)
Cel + Opl
Altered basaltic fragments
Cel ± Opl ± mineral fragments
R7
X 55 15.0kV COMPO NOR WD 10.7mm 21:32:26
100μm KNU 7/2/2019

FIGURE 9

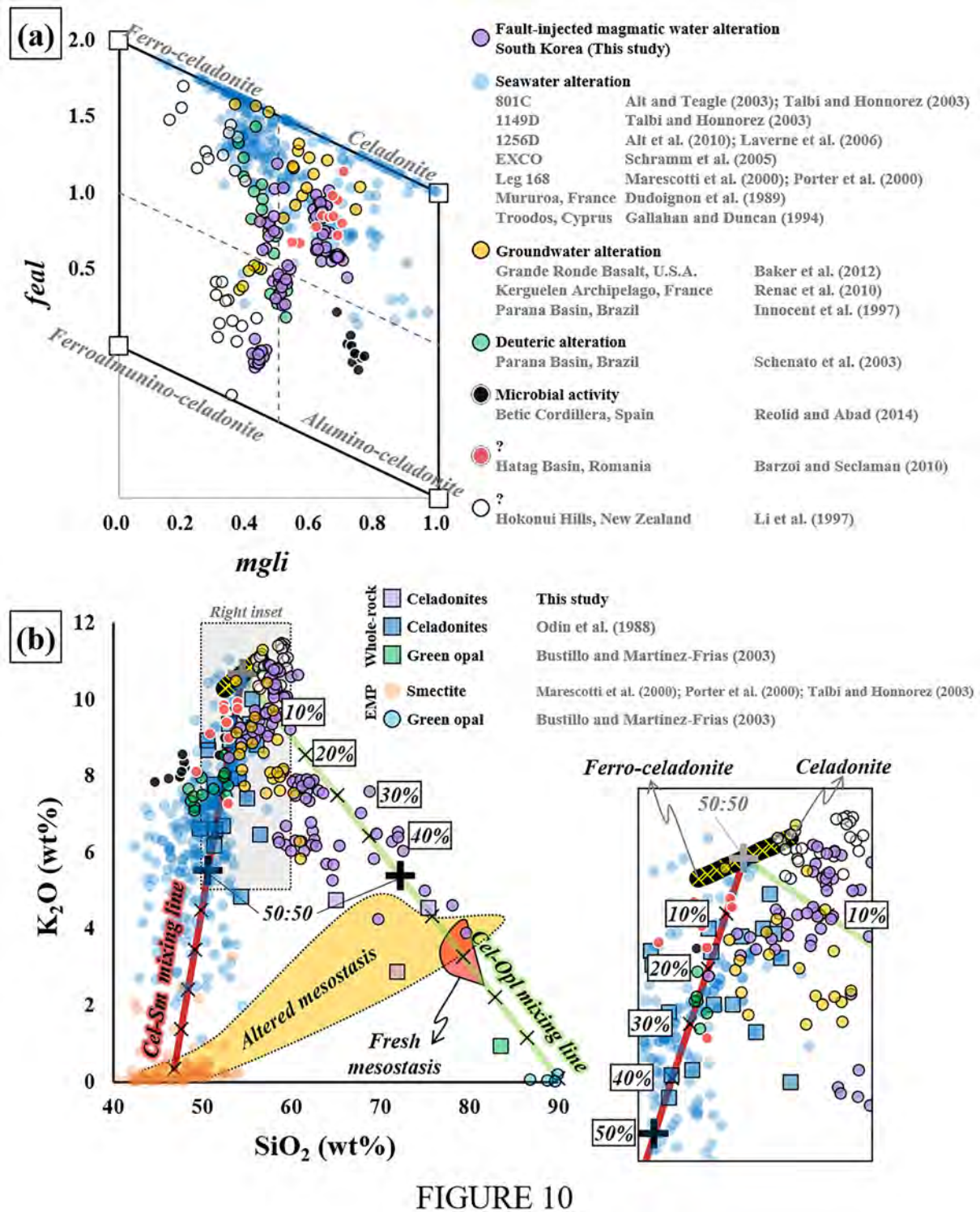
(a)
Ferro-celadonite
Celadonite
Ferroalmunino-celadonite
Alumino-celadonite
feal
mgli
0.0
0.2
0.4
0.6
0.8
1.0
0.5
1.5
2.0
Fault-injected magmatic water alteration
South Korea (This study)
Seawater alteration
801C Alt and Teagle (2003); Talbi and Honnorez (2003)
1149D Talbi and Honnorez (2003)
1256D Alt et al. (2010); Laverne et al. (2006)
EXCO Schramm et al. (2005)
Leg 168 Marescotti et al. (2000); Porter et al. (2000)
Mururoa, France Dudoignon et al. (1989)
Troodos, Cyprus Gallahan and Duncan (1994)
Groundwater alteration
Grande Ronde Basalt, U.S.A. Baker et al. (2012)
Kerguelen Archipelago, France Renac et al. (2010)
Parana Basin, Brazil Innocent et al. (1997)
Deuteric alteration
Parana Basin, Brazil Schenato et al. (2003)
Microbial activity
Betic Cordillera, Spain Reolid and Abad (2014)
?
Hatag Basin, Romania Barzoi and Seclaman (2010)
?
Hokonui Hills, New Zealand Li et al. (1997)
(b)
Right inset
Whole-rock
Celadonites This study
Celadonites Odin et al. (1988)
Green opal Bustillo and Martinez-Frias (2003)
EMP
Smectite Marescotti et al. (2000); Porter et al. (2000); Talbi and Honnorez (2003)
Green opal Bustillo and Martinez-Frias (2003)
10%
20%
30%
40%
50:50
Cel-Sm mixing line
Altered mesostasis
Fresh mesostasis
Cel-Opl mixing line
K2O (wt%)
SiO2 (wt%)
0
2
4
6
8
10
12
40
50
60
70
80
90
Ferro-celadonite
Celadonite
50:50
10%
20%
30%
40%
50%

FIGURE 10

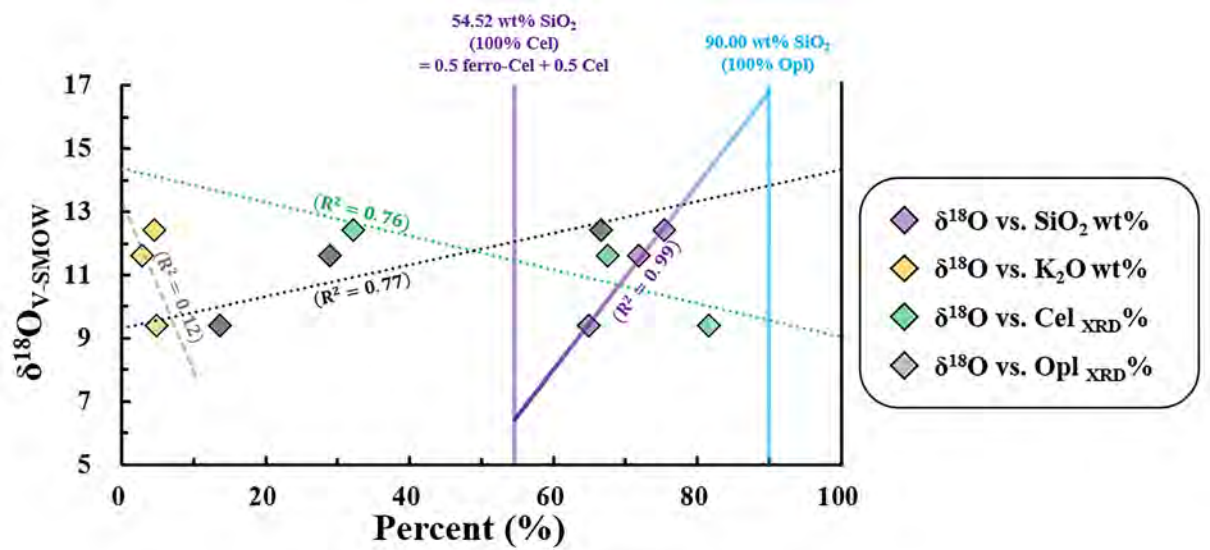
54.52 wt% SiO2
(100% Cel)
= 0.5 ferro-Cel + 0.5 Cel
90.00 wt% SiO2
(100% Opl)
δ18OV-SMOW
Percent (%)
(R2 = 0.76)
(R2 = 0.12)
(R2 = 0.77)
(R2 = 0.99)
δ18O vs. SiO2 wt%
δ18O vs. K2O wt%
δ18O vs. Cel XRD%
δ18O vs. Opl XRD%

FIGURE 11

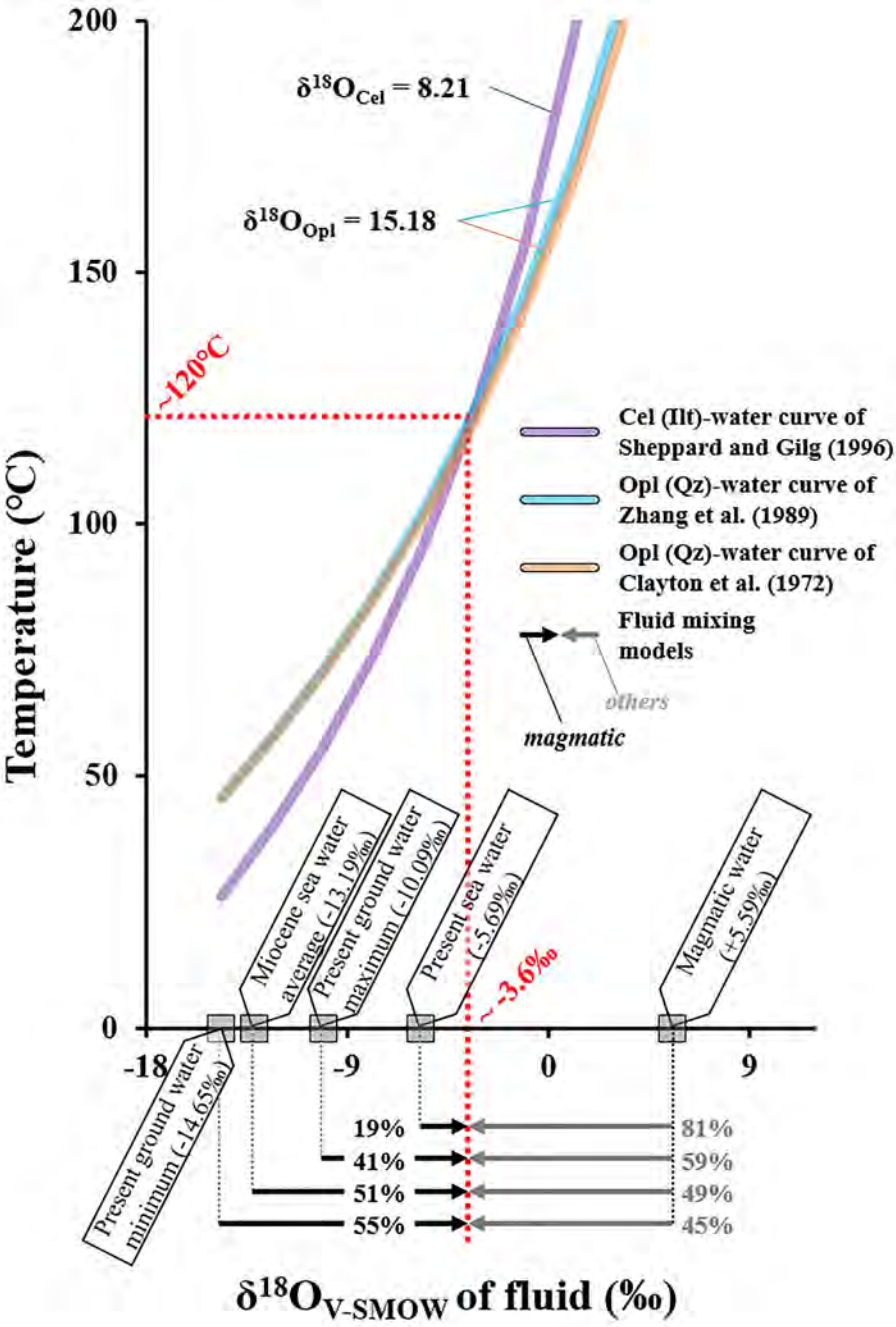
200
150
100
50
0
Temperature (°C)
δ18OCel = 8.21
δ18OOpl = 15.18
~120°C
Cel (Ilt)-water curve of Sheppard and Gilg (1996)
Opl (Qz)-water curve of Zhang et al. (1989)
Opl (Qz)-water curve of Clayton et al. (1972)
Fluid mixing models
others
magmatic
Miocene sea water average (-13.19‰)
Present ground water maximum (-10.09‰)
Present sea water (-5.69‰)
~ -3.6‰
Magmatic water (+5.59‰)
Present ground water minimum (-14.65‰)
-18
-9
0
9
19%
41%
51%
55%
81%
59%
49%
45%
δ18OV-SMOW of fluid (‰)

FIGURE 12

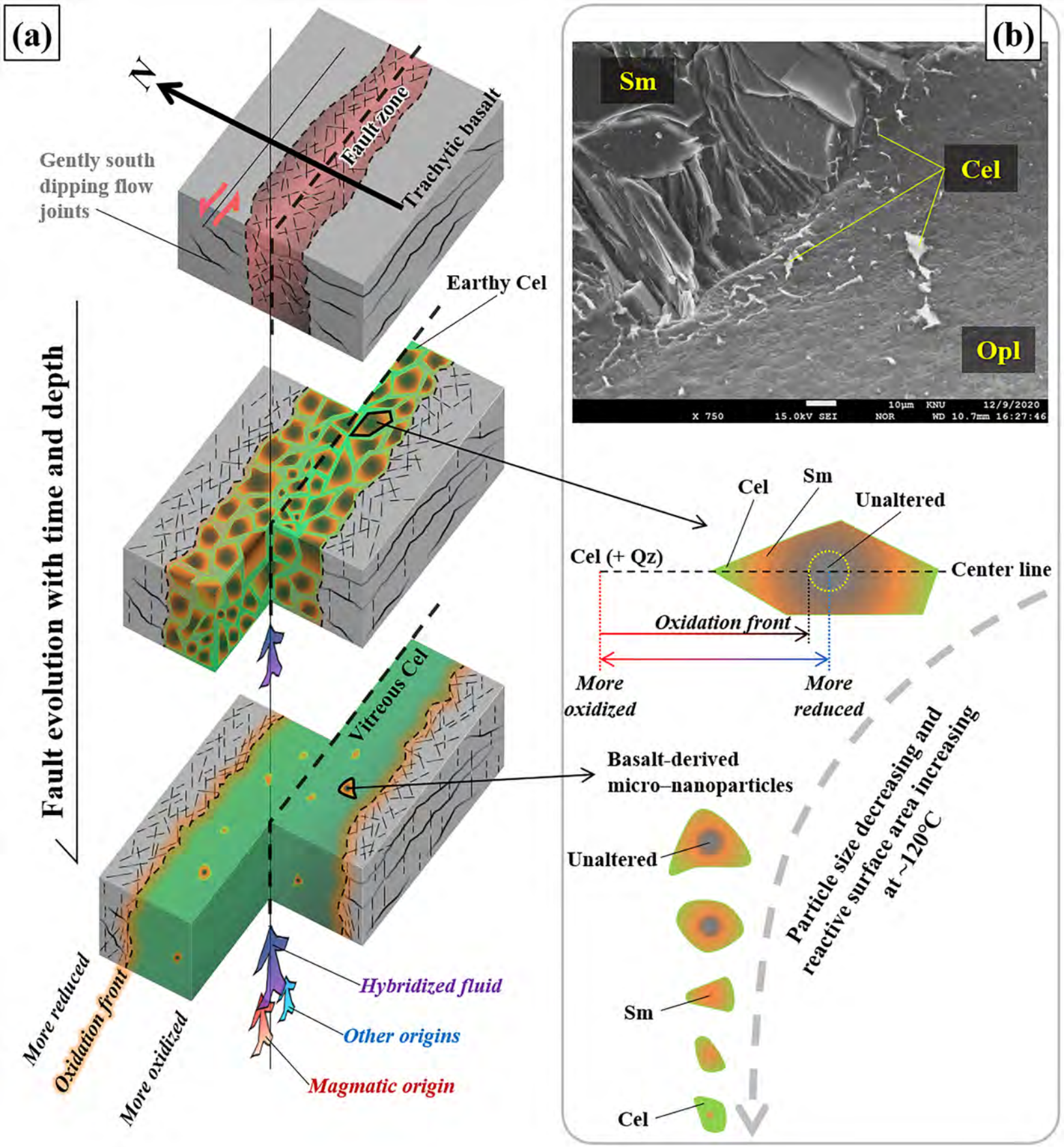
(a)
N
Fault zone
Trachytic basalt
Gently south dipping flow joints
Earthy Cel
Fault evolution with time and depth
Vitreous Cel
More reduced
Oxidation front
More oxidized
Hybridized fluid
Other origins
Magmatic origin
(b)
Sm
Cel
Opl
X 750
15.0kV SEI
10μm
KNU
NOR
12/9/2020
WD 10.7mm 16:27:46
Cel
Sm
Unaltered
Cel (+ Qz)
Center line
Oxidation front
More oxidized
More reduced
Basalt-derived micro–nanoparticles
Unaltered
Sm
Cel
Particle size decreasing and reactive surface area increasing at ~120°C

FIGURE 13